Monthly Notices of the ROYAL ASTRONOMICAL SOCIETY

MNRAS **503,** 3414–3433 (2021) doi:10.1093/mnras/stab608
Advance Access publication 2021 March 4

OMC-1 dust polarization in ALMA Band 7: diagnosing grain alignment mechanisms in the vicinity of Orion Source I

Kate Pattle [1,2★] Shih-Ping Lai [2,3] Melvyn Wright [4] Simon Coudé [5] Richard Plambeck [4] Thiem Hoang [6,11] Ya-Wen Tang [3] Pierre Bastien [7] Chakali Eswaraiah [8] Ray S. Furuya [9] Jihye Hwang [6,11] Shu-ichiro Inutsuka [10] Kee-Tae Kim [6,11] Florian Kirchschlager [12] Woojin Kwon [13,6] Chang Won Lee [6,11] Sheng-Yuan Liu [3] Aran Lyo [6] Nagayoshi Ohashi [3] Mark G. Rawlings [14] Mehrnoosh Tahani [15] Motohide Tamura [16,17,18] Archana Soam [5] Jia-Wei Wang [3] and Derek Ward-Thompson [19]

Affiliations are listed at the end of the paper

Accepted 2021 February 26. Received 2021 February 8; in original form 2020 September 30

ABSTRACT

We present ALMA Band 7 polarization observations of the OMC-1 region of the Orion molecular cloud. We find that the polarization pattern observed in the region is likely to have been significantly altered by the radiation field of the $>10^4\,L_\odot$ high-mass protostar Orion Source I. In the protostar's optically thick disc, polarization is likely to arise from dust self-scattering. In material to the south of Source I – previously identified as a region of 'anomalous' polarization emission – we observe a polarization geometry concentric around Source I. We demonstrate that Source I's extreme luminosity may be sufficient to make the radiative precession time-scale shorter than the Larmor time-scale for moderately large grains ($>$ 0.005–0.1 μm), causing them to precess around the radiation anisotropy vector (k-RATs) rather than the magnetic field direction (B-RATs). This requires relatively unobscured emission from Source I, supporting the hypothesis that emission in this region arises from the cavity wall of the Source I outflow. This is one of the first times that evidence for k-RAT alignment has been found outside of a protostellar disc or AGB star envelope. Alternatively, the grains may remain aligned by B-RATs and trace gas infall on to the Main Ridge. Elsewhere, we largely find the magnetic field geometry to be radial around the BN/KL explosion centre, consistent with previous observations. However, in the Main Ridge, the magnetic field geometry appears to remain consistent with the larger-scale magnetic field, perhaps indicative of the ability of the dense Ridge to resist disruption by the BN/KL explosion.

Key words: techniques: polarimetric – stars: formation – ISM: dust, extinction – ISM: magnetic fields – submillimetre: ISM.

1 INTRODUCTION

The role of magnetic fields in star formation, and particularly in high-mass star formation, remains poorly constrained. Until recently, there was a lack of observational evidence for the magnetic field morphology in the high-density interstellar medium (ISM). Dust emission polarimetry is a long-standing means of inferring ISM magnetic field properties (Davis & Greenstein 1951); however, observations have in the past been strongly surface brightness limited. The polarimetric capabilities of the new generation of submillimetre telescopes, including the Atacama Large Millimeter/submillimeter Array (ALMA), have made magnetic fields in dense, star-forming gas newly accessible (e.g. Cortes et al. 2016; Kwon et al. 2019). However the density regimes now observable have brought with them complications in interpretation of polarization observations, as the mechanisms by which dust grains can gain a preferential alignment proliferate at high densities (Davis & Greenstein 1951; Gold 1952; Lazarian & Hoang 2007a, b; Kataoka et al. 2015; Hoang, Cho & Lazarian 2018; Kataoka, Okuzumi & Tazaki 2019).

Most observations of submillimetre dust polarization at very high densities have been in protostellar discs (e.g. Hull & Zhang 2019, and refs. therein). However, sites of high-mass star formation are another important high-density ISM environment. In this work, we present ALMA Band 7 (340.6 GHz; 881 μm) observations of the OMC-1 region, at the centre of the Orion Molecular Cloud, a nearby site of high-mass star formation (e.g. Bally 2008).

The OMC-1 region, at the centre of the well-studied 'integral filament' in the Orion A molecular cloud, is located at a distance of 388 ± 5 pc (Kounkel et al. 2017), and consists of two dense clumps – the northern Becklin-Neugebauer-Kleinmann-Low (BN/KL) clump (Becklin & Neugebauer 1967; Kleinmann & Low 1967), and the southern Orion S clump (Batria et al. 1983; Haschick & Baan 1989). In this paper, we focus on the centre of the BN/KL clump, an active site of star formation which hosts an extremely powerful wide-angle explosive molecular outflow, with multiple ejecta known as the 'bullets of Orion' (Kwan & Scoville 1976; Allen & Burton 1993). The young stars BN, Source I, and *x*, located in the core of the BN/KL clump, have proper motions consistent with their

★ E-mail: katherine.pattle@nuigalway.ie

having been co-located ∼500 years ago, leading to the suggestion that the BN/KL outflow is the result of a dynamical interaction between these sources (Gómez et al. 2005). The dynamic age of the BN/KL outflow is also ∼500 yr (Zapata et al. 2009), and the kinetic energy released by the interaction is comparable to the energy in the outflow (Kwan & Scoville 1976; Gómez et al. 2005), supporting this interpretation. An alternative explanation for the BN/KL outflow is a protostellar merger (Bally & Zinnecker 2005). Debate over what combination of interaction, decay, and merger produced the BN/KL outflow continues (e.g. Luhman et al. 2017; Farias & Tan 2018); however, the approximate age, high energy, and impulsive nature of the outflow are well established.

Source I drives a separate, slower, bipolar outflow along an axis perpendicular to its direction of motion (Plambeck et al. 2009). BN and Source I appear to be recoiling from a common centre (Rodríguez et al. 2005; Luhman et al. 2017); none the less, the outflow from Source I is symmetric about an axis approximately perpendicular to the direction of motion, despite the significant ram pressure on the source as it ploughs through its surroundings at $\sim 12\,\mathrm{km\,s^{-1}}$ (Rodríguez et al. 2005). This discrepancy could be ascribed to the outflow being shaped by a strong magnetic field. Hirota et al. (2020) recently observed a highly uniform polarization structure in SiO emission associated with the outflow, suggesting a field strength of ∼30 mG, strong enough to prevent distortion of the outflow by ram pressure.

OMC-1 has, on large scales, an hourglass magnetic field (Schleuning 1998; Houde et al. 2004; Pattle et al. 2017; Ward-Thompson et al. 2017). The clump which we observe, in the centre of the OMC-1 region, has an approximately linear magnetic field across it (Chrysostomou et al. 1994, Simpson et al. 2006, Pattle et al. 2017), with an orientation $-64.^{\circ}2 \pm 6.^{\circ}5$ E of N (Ward-Thompson et al. 2017). Estimates of the plane-of-sky field strength in OMC-1 range from $\sim 1 - 10$ mG (Hildebrand et al. 2009; Houde et al. 2009; Pattle et al. 2017), all of which indicate a strong magnetic field.

Complete depolarization is observed on the position of BN/KL in single-dish observations (Schleuning 1998; Houde et al. 2004; Pattle et al. 2017). This depolarization, over a single telescope beam, results from an approximately elliptical polarization pattern in the dense centre of OMC-1, as observed using BIMA (Rao et al. 1998) and the SMA (Tang et al. 2010). In regions where dust grains are aligned with their major axes perpendicular to the magnetic field direction, polarization vectors can be rotated by 90 degrees to trace the plane-of-sky magnetic field (Davis & Greenstein 1951; Andersson, Lazarian & Vaillancourt 2015). Thus Tang et al. (2010), observing the 870 μm dust continuum with the SMA, inferred that the magnetic field in the region is radial, and centred on the outflow. From this they suggested two hypotheses: (1) a toroidal field in a magnetized, differentially rotating 'pseudo-disc' in the centre of OMC-1, or (2) the magnetic field is being dragged into a radially symmetric morphology by the explosive outflow.

OMC-1 has recently been observed in ALMA Bands 3 (3.1 mm) and 6 (1.3 mm) by Cortes et al. (2021). They find a magnetic field of strength 9.4 ± 1.8 mG with a 'quasi-radial' configuration centred on the position of the BN/KL explosion. Their energetics analysis suggests both that the magnetic field is well-coupled to the gas and that the energy in the field is much less than that in the BN/KL explosive outflow, favouring the second of the Tang et al. (2010) hypotheses. In this paper, we present ALMA Band 7 (0.88mm) observations of Source I and its surroundings, a subset of the area observed by Cortes et al. (2021). We investigate whether a single model, or a single grain alignment mechanism, is sufficient to explain the complex polarization morphology observed in the vicinity of Source I.

In recent years, a number of different grain alignment mechanisms have been suggested to explain the polarization properties of dust emission in different environments in the very high-density ISM. As well as the traditional interpretation of polarized dust emission as tracing the plane-of-sky magnetic field direction, an effect usually ascribed to Radiative Alignment Torques (B-RATs; Lazarian & Hoang 2007a; Andersson et al. 2015), alternative mechanisms include supersonic mechanical grain alignment (the Gold effect; Gold 1952), Mechanical Alignment Torques (MATs; Lazarian & Hoang 2007b; Hoang & Lazarian 2016), a variation on Radiative Alignment Torques in which grains precess around the radiation anisotropy vector rather than the magnetic field direction (k-RATs; Lazarian & Hoang 2007a; Tazaki, Lazarian & Nomura 2017), and dust self-scattering (Kataoka et al. 2015). In this work, we will discuss the polarization pattern of the OMC-1 region in the context of these various mechanisms by which polarized emission can arise.

The structure of this paper is as follows: in Section 2, we describe our observations. In Section 3, we interpret the polarization distributions seen across the region. Our conclusions are summarized in Section 4.

2 DATA

We observed three overlapping fields in OMC-1 in ALMA Band 7 polarized light. These observations were taken in ALMA Cycle 6 on 2019 April 9. We observed one track on each source, for a total of 1.5 h of observing time, in array configuration C43-3. The data have project code 2018.1.01162.S. The three fields were centred on the Orion Hot Core, with R.A. (J2000) = $05^h35^m14^s.59$, Dec. (J2000) = $05^{\circ}22'29.''5$; SMA 1, with R.A. (J2000) = $05^h35^m14^s.50$, Dec. (J2000) = $05^{\circ}22'33.''5$; and the Northwest Clump, with R.A. (J2000) = $05^h35^m14^s.11$, Dec. (J2000) = $05^{\circ}22'28.''3$.

The central sky frequency of the observations of each field is 340.7 GHz (881 μm). We observed four spectral windows, three continuum (spw0-2) and one line (spw3). The three continuum windows have central frequencies of 333.8 GHz (899 μm), 335.6 GHz (894 μm) and 347.6 GHz (863 μm), and effective bandwidths of 2000 MHz. The spectral line window has a central frequency of 345.8 GHz (868 μm), with an effective bandwidth of 1875 MHz, and a channel width of 3.906 MHz. The spectral line window is centred on the ^{12}CO $J = 3 \rightarrow 2$ line, as discussed below.

The data were calibrated and imaged using CASA version 5.4.0, using imaging scripts supplied by the Observatory. The phase calibrator was J0529-0519 and the polarization calibrator was J0522-3627. The *tclean* parameters used for imaging were Briggs weighting, with a robust parameter of 0.5, and a cell size of $0.060''$. The output maps have a restoring beam size of $0.54'' \times 0.43''$, oriented -74° E of N, and a maximum recovered size scale of $4.7''$. Integrated Stokes Q, U and I maps were produced using the data from spectral windows spw0-2; note that we do not consider circular polarization (Stokes V) in this work.

Emission from OMC-1 includes contributions from a plethora of spectral lines (e.g. Pagani et al. 2017). Fortunately for our purposes, most of these lines contribute little polarized signal, and so our Stokes Q and U maps made from spw0-2 are dominated by continuum emission. The most significant spectral line in our set of spectral windows is the ^{12}CO $J = 3 \rightarrow 2$ line at 345.8 GHz, on which spw3 is centred. CO emission in outflows can be polarized up to a maximum of ∼3 per cent by the Goldreich-Kylafis effect (GK effect; Goldreich & Kylafis 1982; Ching et al. 2016), which has previously been observed in OMC-1 (Houde et al. 2013). Data from the spectral window dedicated to imaging this line (spw3) is therefore

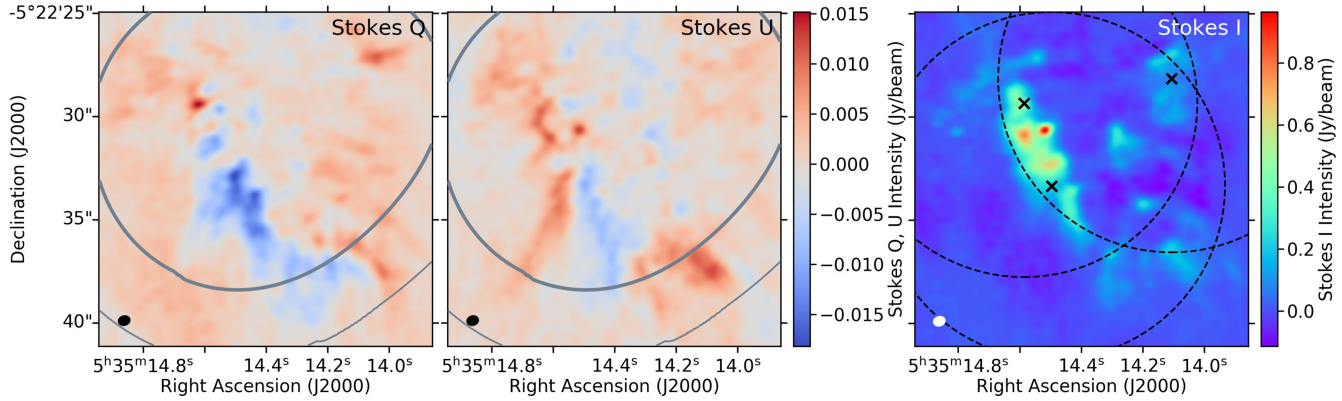

Figure 1. Mosaicked Stokes Q (left), U (centre) and I (right) maps ALMA Band 7 (340.6 GHz, 881 μm) maps of OMC-1. The synthesized beam is shown in the lower left-hand corner of each plot. The 50 per cent (HPBW) and 90 per cent gain contours of the combined primary beam are shown as thin and thick grey lines respectively in the left and centre panels. The centres of our three fields are marked with crosses on the right-hand panel, and their primary beam HPBWs ($16.8''$) are marked with dashed lines.

not considered in this work. We will analyse CO line polarization in OMC-1 in a future work.

We linearly mosaicked our continuum Stokes Q, U and I maps using the Miriad task *linmos* which performs a primary beam weighted mosaic of the three pointing centers to minimize the RMS error. We used the taper option to obtain an approximately uniform noise across the image (Sault, Staveley-Smith & Brouw 1996). The individual images of the three pointings are in good agreement with the resulting mosaic. The effective combined primary beam weighting is shown in Fig. 1. The three pointings are within the FWHM of the primary beam, which minimizes any effects of primary beam off-axis polarization. The mosaicked Q, U and I maps are shown in Fig. 1. Our RMS noise in the mosaicked Stokes Q and U maps is 0.62 mJy/beam. For the purpose of the analysis in Section 3 below, we regridded the Stokes Q, U and I maps to a $0.25''$ pixel grid, approximately Nyquist-sampled on the major axis of the beam.

Polarized intensity is calculated as

$$PI = \sqrt{Q^2 + U^2}, \tag{1}$$

and is shown in Fig. 2. Polarized intensity is thresholded at 6 mJy/beam.

Polarization angle is given by

$$\theta = \frac{1}{2} \arctan\left(\frac{U}{Q}\right). \tag{2}$$

Polarization angles are shown in Fig. 3. We note that while polarization angle segments are referred to as vectors for convenience, they are not true vectors due to the $\pm 180°$ ambiguity in polarization direction. The polarization geometry which we observe is in qualitative agreement with recent Band 3 and and Band 6 results at comparable resolution (Cortes et al. 2021).

When RMS uncertainties on Stokes Q and U emission are equal, uncertainty on polarization angle is given in radians by

$$\delta\theta = \frac{1}{2}\frac{\delta Q}{PI}. \tag{3}$$

For $\delta Q = \delta U = 0.62$ mJy/beam and $PI \geq 6$ mJy/beam, $\delta\theta \leq 3.0°$.

We do not calculate polarization fractions in this work, as the Stokes$I$ map is much more dynamic-range-limited than are the Stokes Q and U maps, as shown in Fig. 2, and so any calculation of polarization fraction is likely to produce artificially large values, particularly in low-surface-brightness regions.

3 RESULTS AND DISCUSSION

Throughout most of the ISM, polarized dust emission can be reliably assumed to arise from dust grains aligned with their major axis perpendicular to the magnetic field direction; the leading theory for explaining which is Radiative Alignment Torques (B-RATs; Lazarian & Hoang 2007a). However, at extremely high densities, such as those found in the centre of OMC-1, this assumption starts to break down. In extreme environments such as these, possible cause of polarized dust emission include: (1) Alignment by B-RATs, the standard mechanism throughout the ISM. (2) Dust self-scattering, an effect seen in protoplanetary discs, in which polarization arises from Rayleigh scattering from large dust grains (Kataoka et al. 2015). (3) Gold alignment: mechanical alignment of dust grains in a supersonic gas flow, with grain major axes parallel to the flow direction (Gold 1952). (4) Mechanical alignment torques (MATs; Lazarian & Hoang 2007b), with grain major axes aligned (a) perpendicular to magnetic field direction (B-MATs, Hoang et al. 2018), (b) with grain major axes perpendicular to gas/dust drift direction (v-MATs, Hoang et al. 2018; Kataoka et al. 2019), (5) alignment by Radiative Alignment Torques such that grain major axes are perpendicular to local radiation gradient (k-RATs; Lazarian & Hoang 2007a; Tazaki et al. 2017). We consider these alternatives when interpreting the polarized emission from dust in OMC-1, introducing each mechanism in detail as it arises.

When considering possible causes of polarized emission in OMC-1, we divided the regions into the following sub-regions: (1) Source I, (2) the Anomalous Region, also referred to as the Fork, (3) the Ridge, (4) MF4/MF5, (5) the Compact Ridge, also referred to as MF1. These sub-regions are labelled on Fig. 2. The mean and median polarization angles, as well as the number of independent measurements, in each region are listed in Table 1. We discuss each region in turn below.

Throughout the following discussion, we principally compare the polarization geometry in each region to three models: polarization arising from grains aligned (1) with their major axes perpendicular to the large-scale 116° E of N magnetic field (polarization angle 26° E of N) observed on larger scales in the region, (2) such that their major axes trace concentric circles around the centre of the BN/KL explosion, and (3) such that their major axes trace concentric circles around Source I. In case (1) we expect to find some variation from the large-scale mean field direction, which is measured at resolutions $\gtrsim 10''$ (Houde et al. 2004; Ward-Thompson et al. 2017), but use the

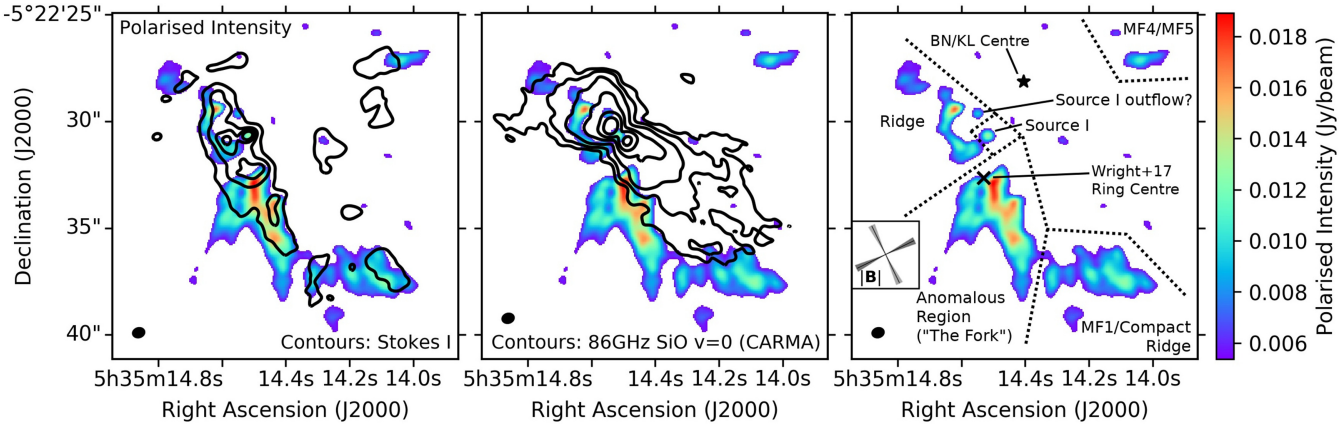

Figure 2. Mosaicked polarized intensity map of OMC 1. Left-hand panel: Polarized intensity overlaid with contours of total intensity (Stokes *I*). Contour levels are 0.1, 0.3, 0.5 and 0.7 Jy/beam. Note that the Stokes*I* map is more dynamic-range-limited than is the polarized intensity map. Centre: Polarized intensity overlaid with contours of CARMA 86 GHz SiO $v = 0$ emission averaged over the velocity range -10 to $+20\,\mathrm{km\,s^{-1}}$, tracing the Source I outflow (Plambeck et al. 2009). Contour levels are 0.05, 0.1, 0.2, 0.5, 1.0, and 2.0 Jy/CARMA beam. Right-hand panel: An illustration of the division of regions in OMC-1 used in this work. The centre of the BN/KL explosion (Rodríguez et al. 2017) is marked with a black star and the centre of the Wright & Plambeck (2017) ring feature is marked with a black cross. The mean magnetic field direction observed on large scales ($115.8 \pm 6.5^\circ$ E of N) is shown in the inset box as a vector with a dark grey wedge indicating uncertainty, and its associated polarization direction ($25.8 \pm 6.5^\circ$ E of N) is shown as a vector with a light grey wedge. In each panel, the synthesized beam is shown in the lower left-hand corner.

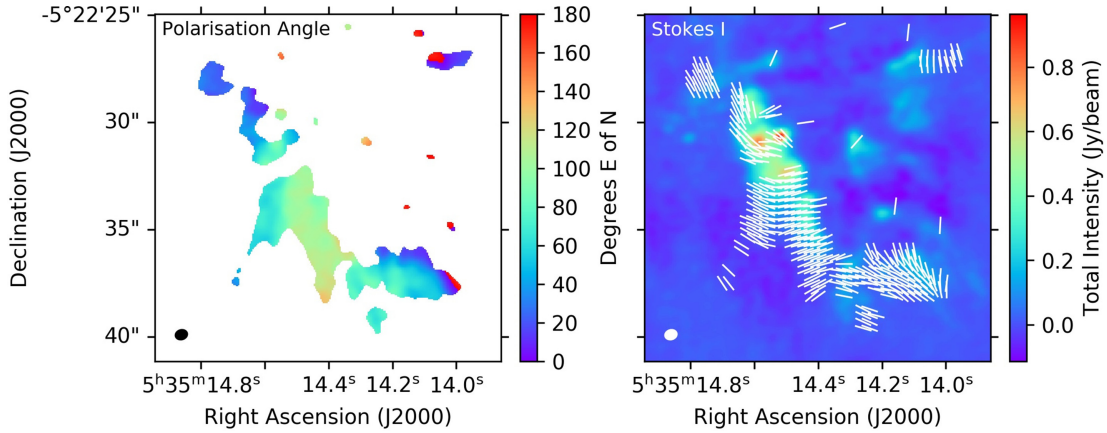

Figure 3. Polarization angle measurements in OMC-1 determined from mosaicked Q and U maps. Left-hand panel: polarization angle, in degrees E of N, mapped to the range $0 \leq \theta < 180$ deg. Right-hand panel: Polarization vectors, plotted on total intensity (Stokes *I*) map. In both panels, the synthesized beam is shown in the lower left-hand corner.

Table 1. Sub-region polarization angle statistics. Angles are given in degrees E of N. Number of independent beams is calculated as the ratio of observed area to beam area.

Sub-region	Mean (deg)	Median (deg)	Independent Beams
Source I	53.5 ± 8.6	52.0 ± 5.4	<2
Anomalous Region/Fork	93.7 ± 19.8	−88.0 ± 8.7	55
Main ridge	41.1 ± 25.7	29.4 ± 9.6	23
MF4/MF5[a]	6.7 ± 8.3	7.7 ± 7.1	6
Compact ridge/MF1[a]	57.2 ± 28.9	58.9 ± 15.1	40

Note.[a] 'MF' refers to methyl formate peaks identified by Favre et al. (2011).

mean direction as a simple model for purposes of comparison. We also consider the dust self-scattering model for Source I, as discussed below.

3.1 Source I

Source I is a well-studied highly luminous high-mass protostar with a collimated SiO outflow (e.g. Hirota et al. 2015), as shown in Fig. 2. Its mass has been a matter of discussion, with its velocity, approximately half that of the $10\,M_\odot$ B star BN, from which Source I appears to be recoiling, suggesting a mass $\sim 20\,M_\odot$ (Rodríguez et al. 2005), while high angular resolution observations of the rotation curves of H_2O and salt lines imply a central mass of $15 M_\odot$ (Ginsburg et al. 2018), as does recent analysis of the combined proper motions of Sources BN, I and *x* (Bally et al. 2020). However, rotation curves of emission lines from the base of the bipolar outflow suggest a mass in the range ~ 5–$8\,M_\odot$ (Kim et al. 2008; Matthews et al. 2010; Plambeck & Wright 2016; Hirota et al. 2017; Kim et al. 2019). Moreover, the high velocity of the source with respect to the surrounding dense medium is belied by the symmetry of its outflow, which would be expected to be significantly bowed by ram pressure (Hirota et al. 2020). These apparent contradictions have recently been reconciled by polarization observations of the SiO emission associated with

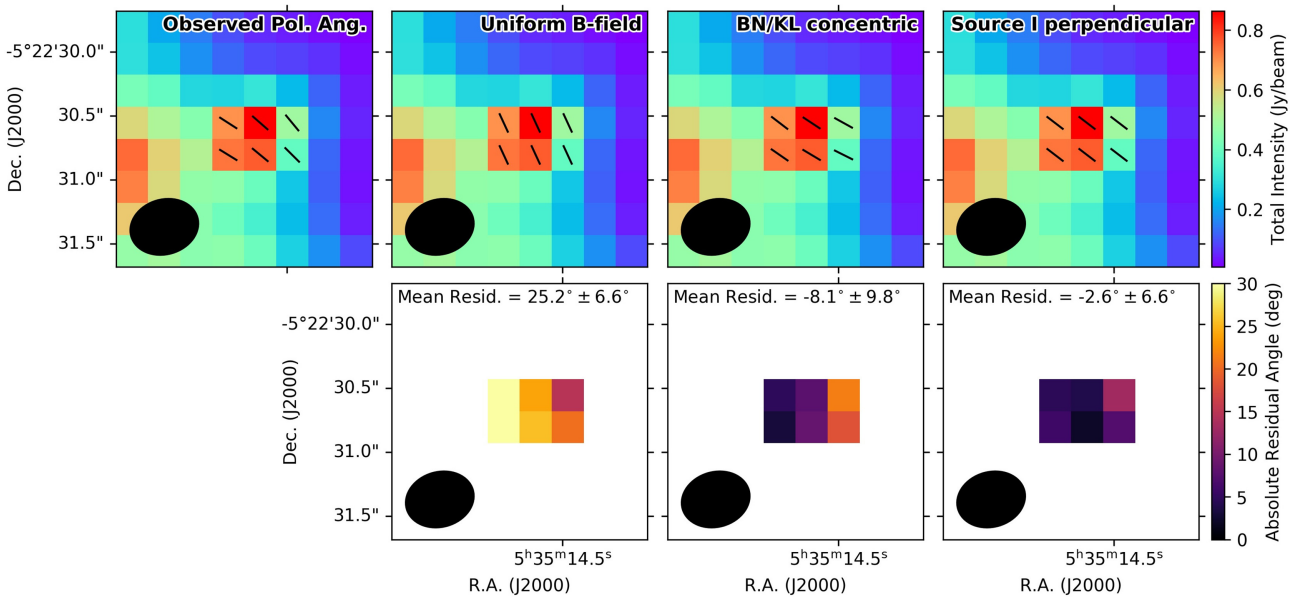

Figure 4. Comparison of models in Source I. Top row shows observed and model polarization geometries, plotted on Stokes *I* emission, bottom row shows absolute difference in angle between data and models. Far left: Observed polarization vectors. Centre left: polarization vectors aligned 26° E of N, perpendicular to the the large-scale magnetic field direction (hypothesized alignment mechanism: B-RATs). Centre right: polarization vectors concentric around the BN/KL explosion centre (hypothesized alignment mechanism: B-RATs/v-MATs). Far right: polarization vectors perpendicular to the major axis of the Source I disc (parallel to minor axis; polarization hypothesized to arise from dust self-scattering). In the bottom row, the colour table saturates at a difference in angle of 30°, to emphasize the differences between the models. All maps are shown on 0.25″ (approximately Nyquist-sampled) pixels. The synthesized beam size is shown in the lower left-hand corner of each plot.

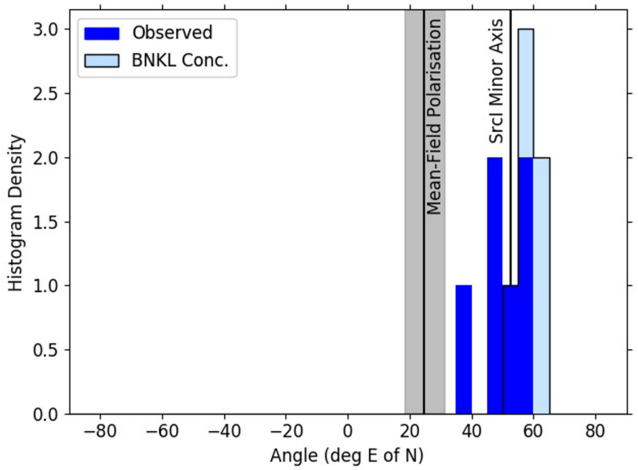

Figure 5. Histogram of polarization angles in Source I (blue), compared with model polarization vectors concentric around the centre of the BN/KL explosion (light blue, solid outline), measured on 0.25″ (approximately Nyquist-sampled) pixels. The polarization angle associated with the mean 116-degree magnetic field direction is marked, as is the angle of the minor axis of the Source I disc.

the outflow, suggesting a magnetic field sufficiently strong to shape the bipolar outflow and to cause sub-Keplerian gas dynamics at the base of the outflow, leading to the mass underestimate (Hirota et al. 2020).

The polarization geometry of Source I is shown in Figs 4 and 5. Source I is effectively unresolved in our observations. We associate six Nyquist-sampled pixels (less than two independent measurements) with the source. The disc itself, with physical size ∼100 au (Ginsburg et al. 2018) and a major axis of 0.23″ at 340 GHz (Wright et al. 2020) is smaller than the beam. The mean polarization angle of Source I over those six pixels is 53°.5 ± 8°.6, and the median is 52°.0 ± 5°.4, inconsistent with the polarization having arisen from a 116° ± 6.5° magnetic field, but consistent with being parallel to the minor axis of Source I (53°; Ginsburg et al. 2018). The polarization direction which we observe is also broadly consistent with that expected for a polarization pattern concentric around BN/KL. The three model geometries which we consider for Source I are shown in Fig. 4.

Kataoka et al. (2015) introduced the dust self-scattering mechanism for producing polarized emission in protostellar discs, wherein polarization arising at a given wavelength arises from Rayleigh scattering from dust grains with sizes comparable to that wavelength. This mechanism can produce a polarization pattern concentric around the protostellar position, or aligned with the disc minor axis, consistent with what we see in Source I. The conditions for polarization arising from dust self-scattering to produce uniform polarization aligned with the disc minor axis, as seen in Source I, are given by Sadavoy et al. (2019) as an inclined (i>60°) disc with optically thick dust emission.

Wright et al. (2020) find a spectral index ∼2 along the disc midplane consistent with optically thick dust emission. This spectral index increases to ∼3 at the disc edges, suggesting that dust emission is optically thin in the periphery of the disc. Wright et al. (2020), observing at 340 GHz, set a lower limit to the disc inclination of 79° ± 1° (with major and minor axes 99 × 19 au) at a disc brightness temperature contour of 400 K, and 74° ± 1° (239 × 45 au) at a disc brightness temperature contour of 25K, but note that the observed geometry suggests that the inclination is closer to 90°. Similarly, Matthews et al. (2010) measure an inclination ∼85° from SiO masers close to the disc. Source I thus meets the conditions for our observed

average polarization direction to arise from dust self-scattering. While we note that the polarization geometry is also consistent with being concentric around BN/KL, dust self-scattering is an established mechanism for producing polarization in protostellar discs, the necessary conditions for which are matched in Source I, and so we consider it to be the probable source of the dust polarization which we observe. This implies the existence of significant dust growth and coagulation within the Source I disc. While grain growth is expected in protostellar discs (e.g. Kwon et al. 2009), for dust self-scattering to be observed, there must be a significant population of spherical dust grains with size $\sim\lambda/2\pi$ (Kataoka et al. 2015), or nonspherical grains with sizes $\gtrsim \lambda/2\pi$ (Kirchschlager & Bertrang 2020). At 870 μm, this implies the existence of a population of dust grains with sizes $\sim$ 140 μm or larger in the Source I disc.

We note that Hirota et al. (2020) found an upper limit continuum polarization fraction of 1 per cent in the Source I disc at 96 GHz (3.1 mm). These observations, with a synthesized beam size of $0.05''$, did resolve the Source I disc, and so if scattering were important, some polarization signal would be expected. If scattering is significant at 345 GHz but negligible at 96 GHz, this puts strong constraints on the grain size distribution in the Source I disc, with a significant population of grains with sizes $\sim$ 140 μm, but a cut-off in grain size at $<$ 500 μm. Resolved polarization observations of Source I at 345 GHz are required to confirm the dust self-scattering hypothesis, and to better constrain the grain size distribution in the disc.

3.2 Anomalous Region/Fork

There is a significant 'fork' visible to the south of the Hot Core in the polarized intensity and polarization angle maps, as shown in Figs 2 and 3. Vectors on the western side of the fork have a typical polarization angle significantly different both to that across the Ridge and to that in the eastern arm. Rao et al. (1998), observing OMC-1 in polarized light with BIMA, identified this as an 'anomalous region', with polarization vectors significantly different from elsewhere in OMC-1, and inconsistent with being perpendicular to the large-scale field direction. The vectors which we see are consistent with their observations. Rao et al. (1998) suggested that grains in this region are mechanically aligned by the Gold effect, driven by the Source I outflow.[1]

Wright & Plambeck (2017) suggest that much of the dust emission in the Fork originates from the walls of the cavity formed by the bipolar outflow from Source I, based on the spatial coincidence of dust emission and SiO emission tracing the outflow. The Source I outflow is shown in Fig. 2 In the following discussion we consider both the case in which emission arises from the outflow cavity wall, and that in which it arises from the ambient medium of OMC-1.

3.2.1 Comparison of data and models

Figs 6 and 7 show that the polarization vectors in the Fork are inconsistent with the 26° polarization direction associated with the large-scale magnetic field, but broadly consistent with being concentric around either the BN/KL explosion centre, the centre of a 'ring feature' identified by Wright & Plambeck (2017) (discussed below), or Source I. Fig. 6 shows each of these polarization geometries, along with the absolute residual angles between the models and the observed polarization geometry. The BN/KL-concentric model is broadly consistent with the observations in the eastern arm of the Fork, but systematically different by $\sim$20° in the western arm. The ring-feature-concentric model is consistent with the observations in the south of the region, but not consistent in the north; we discuss this further below. The Source I-concentric model is broadly consistent with the observed polarization geometry in the western arm of the Fork.

We quantified the similarity of these models to the data using two-sided Kolmorogov-Smirnov (KS) and Kuiper tests. We chose the KS test as the most widely used statistic for comparing the similarity of two distributions, and the Kuiper test as a more appropriate measure of similarity for distributions of cyclic variables (e.g. Aizawa et al. 2020).

For each model, we determined polarization angles predicted in each pixel by the model, and drew sets of perturbations on these angles from a Gaussian distribution of width σ_θ. We then performed two-sided KS and Kuiper tests comparing the model, with added dispersion in angle, to the data. We repeated this process 1000 times for each value of σ_θ considered. We tested σ_θ values in the range 1−20°. Additional dispersion in angle over our measured uncertainties ($\delta\theta < 3°$) could result from Alfvénic distortion of the magnetic field by non-thermal gas motions (Davis 1951; Chandrasekhar & Fermi 1953). The results of these tests are shown in Fig. 8.

According to both tests, the BN/KL-concentric model is the only model that can be made consistent ($p > 0.05$) with the data in the eastern arm, while the Source-I-concentric model is the only model that can be made consistent with the data in the western arm. The two tests produce similar results, with the Kuiper test generally returning a more narrow range of angles over which the model and the data agree with a probability $p > 0.05$.

In the eastern arm, the observed polarization geometry is consistent with the Cortes et al. (2021) model in which the magnetic field is radial around BN/KL; however, additional scatter in the observed polarization angle above our observed uncertainty must be introduced. The best agreement between the BN/KL-concentric model and our data occurs for $\sigma_\theta = 8°$, but $p > 0.05$ agreement occurs up to $\sigma_\theta \approx 13°$ (KS test), or in the range $4.5° \lesssim \sigma_\theta \lesssim 12.5°$ (Kuiper test).

In the western arm, $p > 0.05$ agreement between the Source-I-concentric model and our data occurs at $\sigma_\theta < 8°$ (KS test), or $\sigma_\theta < 5°$ (Kuiper test). The difference in modelled angle dispersion between the eastern and western arms of the Fork – and between the western arm and elsewhere in OMC-1, as described below – is suggestive either of different non-thermal gas motions within the western arm, or of a different alignment mechanism between the two arms.

We consider five hypotheses to explain the observed polarization pattern in the western arm: (1) grains aligned by B-RATs with respect to a distorted magnetic field; (2) polarization arising from scattering of emission from Source I; (3) polarization arising from supersonic mechanical alignment (Gold alignment) induced by either the BN/KL explosion or the Source I outflow; (4) grains aligned by subsonic v-MATs, induced by (a) the shock associated with the passage of ejecta from the BN/KL explosion through the region; (b) shocks associated with the Source I outflow; (5) grains aligned by k-RATs, perpendicular to the radiation gradient associated with Source I. We consider these hypotheses in turn below, and then as a check on our analysis confirm that the gas damping timescale is sufficiently long in the region to allow a preferential dust precession axis to exist. The following discussion is summarized in Table 2.

[1]The 'outflow' referred to by Rao et al. (1998) is now recognized to be high-velocity gas from the BN/KL explosive event.

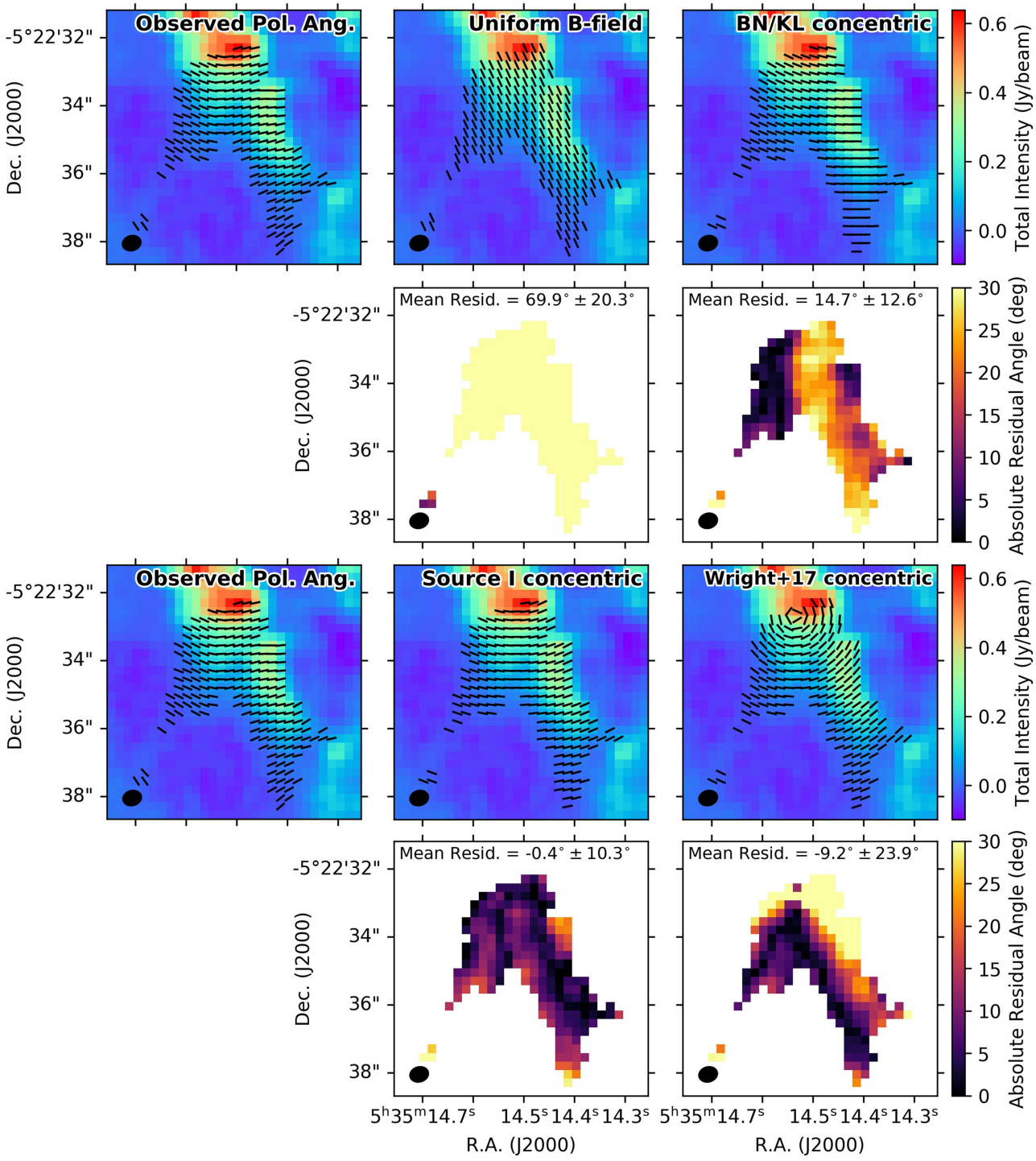

Figure 6. Comparison of models in the Anomalous Region/Fork. First and third rows show observed and model polarization geometries, plotted on Stokes*I*emission, second and fourth show absolute difference in angle between data and models. Left–hand column shows observed polarization vectors. Central column shows polarization vectors perpendicular to the large-scale magnetic field direction (top; alignment mechanism: B-RATs) and concentric around Source I (bottom; hypothesized alignment mechanism: k-RATs). Right-hand column shows polarization vectors concentric around the BN/KL explosion centre (top; hypothesized alignment mechanism: B-RATs/v-MATs) and concentric around the centre of the Wright & Plambeck (2017) ring feature (bottom; hypothesized alignment mechanism: v-MATs). In the second and fourth rows, the colour table saturates at a difference in angle of 30°, to emphasize the differences between the models. All maps are shown on 0.25″ (approximately Nyquist-sampled) pixels. The synthesized beam size is shown in the lower left-hand corner of each plot.

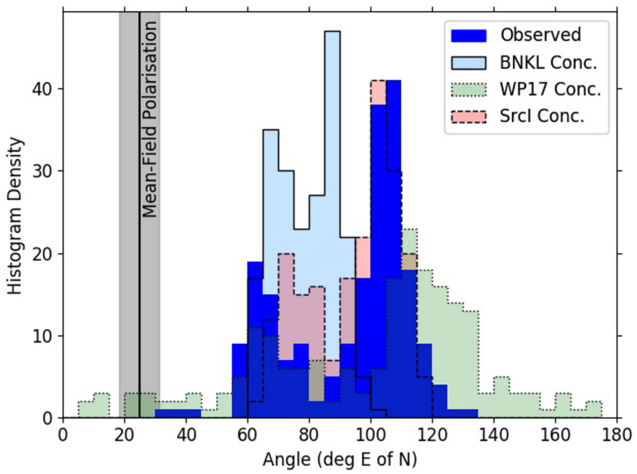

Figure 7. Histogram of observed polarization angles in the Anomalous Region/Fork (blue), compared with models: polarization vectors concentric around (1) the centre of the BN/KL explosion (light blue, solid outline), (2) the centre of the Wright & Plambeck (2017) ring feature (green, dotted outline), (3) Source I (red, dashed outline). The polarization angle associated with the mean 116-degree magnetic field direction is marked. Polarization angles are measured on 0.25″ (approximately Nyquist-sampled) pixels and shown in the range 0–180 degrees for clarity.

3.2.2 *Distorted magnetic field*

As shown in Figs 6 and 7, the polarization pattern in the western arm of the Fork is inconsistent with that predicted based on the large-scale mean field direction and with the radial field geometry observed elsewhere in OMC-1 by Tang et al. (2010) and Cortes et al. (2021). Tang et al. (2010) hypothesized that the polarization geometry of OMC-1, observed at 870 μm using the SMA, arose from grains aligned perpendicular to a magnetic field which had been significantly distorted from its initial configuration. They proposed two hypotheses for how the field had been distorted: (1) that the observed polarization indicated that the density structure of the centre of OMC-1 forms a rotating 'pseudo-disc' around the centre of the BN/KL explosion, with a toroidal magnetic field. We consider this hypothesis to have been disfavoured by ALMA studies better determining the line-of-sight distances and velocities of the various OMC-1 clumps (Pagani et al. 2017). (2) that the BN/KL explosive outflows have realigned the magnetic field to be radial around the explosion centre (i.e. polarization vectors are concentric around the BN/KL centre). Our observations suggest that the vectors in OMC-1, including in the eastern arm of the Fork, are mostly consistent with being concentric around the BN/KL explosion centre. However, in the western arm, the polarization geometry which we observe is more consistent with being concentric around Source I, suggesting that if the grains remain aligned with the magnetic field in the region, the field is likely to be radial around that source. This could potentially indicate a highly poloidal field in the Source I outflow, or the magnetic field being well-coupled to infalling or outflowing gas.

3.2.3 *Larmor time-scale*

We will consider alternative explanations for the observed polarization geometry in the western arm of the Fork, which do not require such wholesale reorganization of the magnetic field. For dust grains to be aligned with respect to the magnetic field direction, rather than some other axis, the time-scale for precession around the magnetic field direction (the Larmor time-scale, τ_{Lar}) must be shorter than all other precession time-scales (e.g. Hoang & Lazarian 2016). Therefore, we estimate τ_{Lar} in the western arm of the Fork, for comparison with other time-scales.

The Larmor time-scale is given by Tazaki et al. (2017) as

$$\tau_{Lar} \simeq 1.3\hat{\rho}\hat{s}^{-\frac{2}{3}}a_{-5}^{2}\hat{B}^{-1}\hat{\chi}^{-1}\ \text{year}, \tag{4}$$

where $\hat{\rho} = \rho/3\,\mathrm{g\,cm^{-3}}$ and ρ is the mass density of the grains, $\hat{s} = s/0.5$ and s is the axial ratio of the dust grains, $a_{-5} = a/10^{-5}$ cm and a is the radius of the dust grains, $\hat{\chi} = \chi(0)/10^{-4}$ and $\chi(0)$ is the zero-frequency magnetic susceptibility of the grains, and $\hat{B} = B/5\mu$G, and B is magnetic field strength. We take $\hat{\rho} \sim 1$ and $\hat{s} \sim 1$.

Measurements made on larger scales in the region indicate a magnetic field strength $B \lesssim 10$ mG at densities $n_{\mathrm{H}} \sim 10^{6}\,\mathrm{cm^{-3}}$ (Hildebrand et al. 2009; Houde et al. 2009; Pattle et al. 2017), similar to the ambient density in which Source I is moving (Wright & Plambeck 2017). Cortes et al. (2021) find $B = 9.4 \pm 1.8$ mG at $n_{\mathrm{H_2}} = 2.7 \times 10^{8}\,\mathrm{cm^{-3}}$. The similarity in gas densities between the Fork and the region of OMC-1 in which this magnetic field strength was determined (Favre et al. 2011) and the strong coupling between the magnetic field and the gas in OMC-1 (Cortes et al. 2021) suggest that this value is likely to be representative of the field strength in the Fork, and so we adopt $\hat{B} \sim 2000$. All of these estimates of magnetic field strength were made using variants of the Davis-Chandrasekhar-Fermi (DCF) method (Davis 1951; Chandrasekhar & Fermi 1953).

Draine (1996) gives values for magnetic susceptibility $\chi(0)$ in the range $4.2 \times 10^{-5} - 4.2 \times 10^{-3}$ for paramagnetic grains, and so we take $\hat{\chi} \sim 0.4 - 40$. These combine to give

$$\tau_{Lar} \sim (1.6 \times 10^{-5} - 1.6 \times 10^{-3})\,a_{-5}^{2}\ \text{year}. \tag{5}$$

Cortes et al. (2021) note that their derived magnetic field strength, $B = 9.4 \pm 1.8$ mG, is effectively an upper limit on the true magnetic field strength, due to the beam- and line-of-sight-averaging effects inherent in the DCF method (see, e.g. Pattle & Fissel 2019 for a discussion). Thus, the value of τ_{Lar} given in equation 5 is a lower limit, for our adopted range of χ values. However, we note that if the dust grains in the Fork were to have super-paramagnetic inclusions (e.g. Lazarian & Hoang 2019, and refs. therein), χ could be made considerably larger, correspondingly decreasing τ_{Lar}. The uncertainty on τ_{Lar} is thus difficult to quantify: Cortes et al. (2021) give a formal uncertainty on B of ∼20 per cent, but this is dwarfed by the two orders of magnitude (or larger) uncertainty on χ (Draine 1996), and so we consider only the latter when estimating the range of plausible values of τ_{Lar}.

3.2.4 *Dust self-scattering*

The polarization pattern in the western arm of the Fork is consistent with being concentric around Source I. This could imply that polarization arises from scattering of light from Source I (Kataoka et al. 2015). We note however that as is the case in the Source I disc, this would require grain sizes ∼ 140μm. If the emission from the western arm of the Fork arises from the ambient medium of OMC-1, this level of grain growth appears impossible. If the emission arises from the Source I outflow cavity, and if such large grains exist in the Source I disc as is suggested by the Source I polarization pattern, it could be hypothesized that they might be entrained into the outflow. However, transport of such large dust grains, as well as their avoiding destruction in the outflow in sufficient number to produce

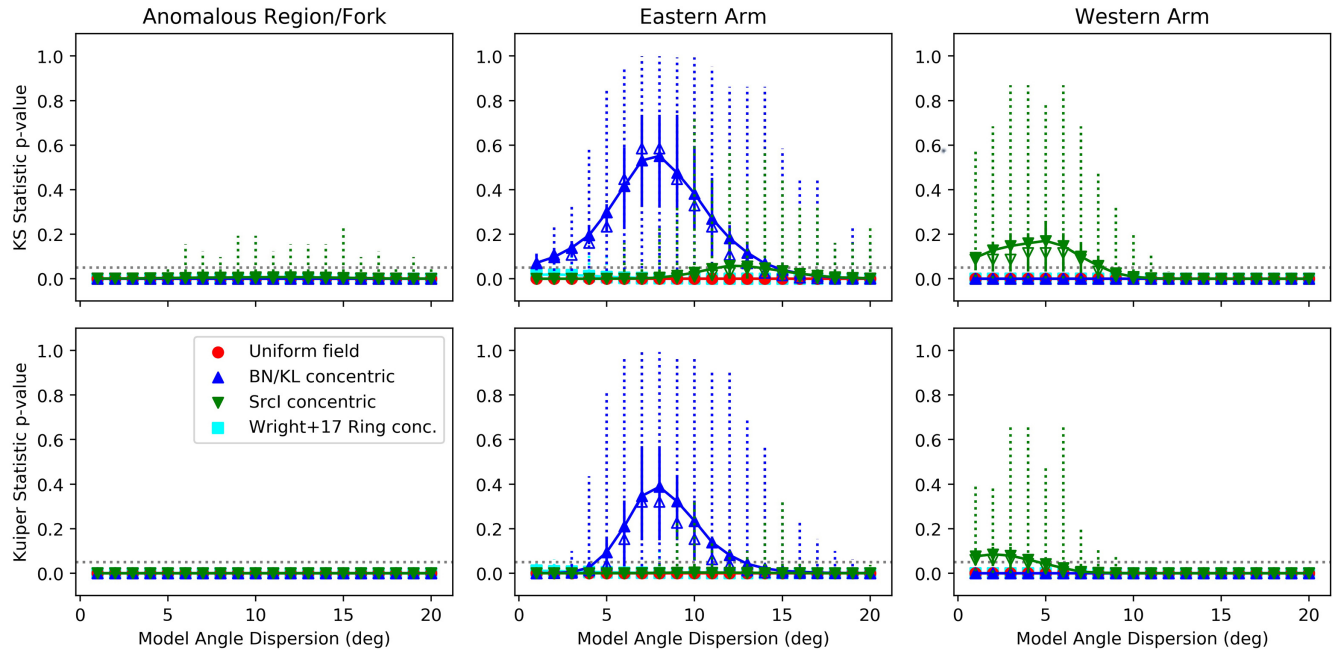

Figure 8. Results of Kolmogorov-Smirnov (KS) and Kuiper tests comparing observed polarization angles in the Anomalous Region/Fork to a set of realizations of our four models with specified values of Gaussian dispersion in polarization angle. Top row shows the p values associated with the KS statistic and bottom row shows those associated with the Kuiper statistic. Left-hand column shows results for the entire Fork; centre column, for the eastern arm; and right-hand column, for the western arm. In each panel, solid symbols show the mean value, open symbols, the median. Dotted error bars show the full range of the p-value across the set of realizations; solid error bars show the interquartile range. The dashed grey line marks the $p = 0.05$ criterion for statistical significance.

Table 2. A summary of potential mechanisms for producing polarized dust emission in the western arm of the Fork. 'AM' (ambient medium) refers to polarization in the Fork arising from the ambient medium of OMC-1; 'OCW' (outflow cavity walls) to polarization arising from the cavity walls of the Source I outflow.

	B-RATs	Dust Self-scattering	Gold Alignment	v-MATs (BN/KL)	v-MATs (Src I outflow)	k-RATs (Src I)
Predicted/observed geometries consistent?	N/A	Yes	No	Marginal	Uncertain	Yes
Polarization arises from ambient medium or Src I outflow cavity walls?	Either	OCW	AM: BN/KL-driven OCW: Src I-driven	AM	OCW	OCW strongly favoured
Required conditions	τ_{Lar} shortest	> 100 μm grains in Src I outflow	$\Delta v > c_s$	τ_{mech} shortest; $\Delta v < c_s$		$\tau_{rad,\,p}$ shortest
Conditions met?	For small grains ($a \lesssim 0.005$–0.1 μm)	Unlikely	Ruled out geometrically	No; requires $\omega \ll \omega_{th}$		For large grains ($a \gtrsim 0.005$–0.1 μm)

the observed polarization pattern, does not seem likely (Giacalone et al. 2019). We thus discount this hypothesis, while noting that we cannot definitively rule it out.

3.2.5 *Supersonic mechanical (Gold) alignment*

For completeness, we note the possibility of supersonic mechanical alignment (Gold alignment; Gold 1952). If the polarized emission in the Fork arises from the ambient medium of OMC-1, and is associated with BN/KL shocks, Gold alignment would produce a radial polarization pattern around the centre of the BN/KL explosion. If the emission in the western arm of the Fork arises from the Source I outflow cavity walls, Gold alignment would produce polarization parallel to the Source I outflow, or radial around Source I. All of these geometries are inconsistent with the observed polarization pattern shown in Fig. 3, and so we do not consider Gold alignment further.

3.2.6 *Mechanical alignment torques*

Lazarian & Hoang (2007b) proposed the mechanical alignment torques (MATs) mechanism, in which grains drifting relative to gas are aligned by mechanical torques to have their long axes perpendicular to the precession axis of the grain. This precession axis is typically the magnetic field direction (B-MATs, Lazarian & Hoang 2007b; Hoang et al. 2018), but can in some environments be the velocity vector of the gas/dust drift (v-MATs, Lazarian & Hoang 2007b; Hoang & Lazarian 2016). The v-MAT alignment mechanism can occur when the velocity difference between the gas and dust is subsonic, and when the mechanical alignment time-scale (the precession time around the gas flow), τ_{mech}, is shorter than the Larmor precession time-scale, τ_{Lar} (cf. Hoang et al. 2018, Section 6.4). This mechanism further requires the dust grains to have significant helicity, which is acquired through coagulation. (Brauer, Dullemond & Henning 2008; Ormel et al. 2009; Hirashita 2012).

Hoang et al. (2018) discuss environments where gas/dust drift is likely to be induced, concluding that such drift may be triggered by cloud–cloud collisions, radiation pressure, ambipolar diffusion, or gravitational sedimentation. Gas/dust drift occurs across shock fronts (McKee et al. 1987), and so can plausibly expected to be occurring in OMC-1, either in the aftermath of the BN/KL explosion, or in shocks within the Source I outflow. Shocks in OMC-1 are thought to be continuous (C-shocks; e.g. Colgan et al. 2007), supporting the hypothesis that the magnetic field in the region is dynamically important (Draine 1980).

If the emission in the Fork arises from the ambient medium of OMC-1, rather than from the Source I outflow cavity walls, we might expect grains to be mechanically aligned by shocks associated with the BN/KL explosion ejecta. While the observed polarization geometry is, in the western arm of the Fork, inconsistent with being concentric around the BN/KL explosion centre, Wright & Plambeck (2017) identified a ring of emission near SMA 1 in HCN 354.5 GHz and H_3CN 354.7 GHz emission, which they interpreted as evidence for passage of debris from the BN/KL explosion. The ring has $\sim$2 km s^{-1} expansion velocity and a dynamical age of $\sim$700 yr, consistent with the approximate age of the BN/KL explosion, if its expansion has been somewhat decelerated. This feature is at a different systemic velocity (+12 km s^{-1}) than is the material which Wright & Plambeck (2017) associate with the Source I outflow (located at -12 to -7 km s^{-1}), and is likely to be located behind the BN/KL explosion centre. As well as considering grain alignment concentric around Source I, we consider grain alignment concentric around the centre of the ring, in case mechanical alignment was induced by the shock associated with these particular ejecta. In the south of the Anomalous Region/Fork (i.e. at larger radii), the polarization pattern is more consistent with being concentric around the position of the ring than it is with being concentric around the BN/KL explosion centre, but the model fails at positions near the ring centre.

Alternatively, if the polarized emission in the Fork arises from the Source I outflow cavity walls, grains cannot be aligned by shocks associated with the BN/KL explosion, as Source I and its associated outflow is moving behind these shock fronts (e.g. Hirota et al. 2020). In this case, v-MAT alignment could instead be induced by shocks associated with the expansion of the bipolar outflow into its surroundings. Polarization vectors might then be expected to be radial around Source I, perpendicular to the surface of the outflow, or less ordered, depending on the nature of the outflow shocks.

3.2.7 *Mechanical alignment time-scale*

The time-scale for alignment by v-MATs is given by

$$\tau_{mech} \simeq 36 \left(\frac{c_s}{\Delta v}\right)^2 \left(\frac{\omega}{\omega_{th}}\right) \hat{s}^2 \frac{1}{\sin 2\Theta} \text{ year}, \quad (6)$$

(Lazarian & Hoang, ApJ subm.), where c_s is gas sound speed, Δv is gas/dust velocity difference, ω is the grain angular velocity, ω_{th} is the thermal angular velocity, and Θ is the angle between the grain axis of major inertia and the direction of radiation. We take $\hat{s} \sim 1$ and $\sin 2\Theta \sim 0.5$.

The velocity difference between gas and dust in C-type shocks is not well characterized, potentially taking any value between zero and the shock velocity, depending on environment (Wardle 1998; Guillet, Pineau Des Forêts & Jones 2007). However, the condition for v-MATs is $\Delta v < c_s$, and so equation (6) becomes

$$\tau_{mech} \gtrsim 72 \left(\frac{\omega}{\omega_{th}}\right) \text{ year}. \quad (7)$$

Comparison of the timescales given by equations 5 and 7 suggests that $\tau_{mech} \gg \tau_{Lar}$. The requirement for $\tau_{mech} < \tau_{Lar}$ to hold is the physically implausible condition $\omega/\omega_{th} \ll 1$, i.e. grains would have to be rotating subthermally. The time-scale for v-MAT alignment thus remains too long for this mechanism to be likely to be the main cause of grain alignment in the Fork.

3.2.8 *Radiative alignment torques*

Under the radiative alignment rorques (RATs) paradigm of grain alignment, grains are efficiently aligned when they can be spun up to suprathermal rotation by an anisotropic radiation field (Dolginov & Mitrofanov 1976; Lazarian & Hoang 2007a). As with MATs, the grains will align with their long axes perpendicular to their precession axis. In the large majority of ISM environments, the precession axis can be presumed to be the magnetic field direction (B-RATs Lazarian & Hoang 2007a). However, in the presence of a sufficiently strong and anisotropic radiation field, the precession axis can instead be the radiation anisotropy vector, and so grains will be aligned with their major axes concentric around the source driving the radiation field (k-RATs; Tazaki et al. 2017). The condition for k-RATs to dominate over B-RATS is that the radiative precession time-scale must be shorter than the Larmor time-scale, i.e. $\tau_{rad,p} < \tau_{Lar}$ (Lazarian & Hoang 2007a; Tazaki et al. 2017). Alignment by k-RATs has not been definitively observed outside of protostellar discs; however, there has been a recent tentative detection in HAWC + observations of the nearby Orion Bar (Chuss et al. 2019), and a potential detection in the envelope of an evolved star (Andersson et al. 2018).

The brightest source in OMC-1 is Source I, with a luminosity $>10^4$ L$_\odot$ (Menten & Reid 1995). As shown in Fig. 6, the polarization pattern in the Fork is quite consistent with being concentric around Source I, potentially suggesting that the dust grains in the region are aligned by k-RATs, driven by the radiation field of Source I. In the following section, we estimate the radiative precession time-scale $\tau_{rad,p}$ arising from the unobscured radiation field of Source I in the Anomalous Region/Fork. We do not include other sources of radiation in OMC-1 in this analysis, as it is the strongly anisotropic radiation field of Source I which we hypothesize is driving k-RAT alignment in the fork.

3.2.9 *Radiative precession time-scale*

The radiative precession time-scale is given by Tazaki et al. (2017) as

$$\tau_{rad,p} \simeq 110\, \hat{\rho}^{\frac{1}{2}} \hat{s}^{-\frac{1}{5}} a_{-5}^{\frac{1}{2}} \hat{T}_d^{\frac{1}{2}} \left(\frac{u_{rad}}{u_{\rm ISRF}}\right)^{-1} \left(\frac{\bar{\lambda}}{1.2\,\mu\text{m}}\right)^{-1} \left(\frac{\gamma |Q_\Gamma|}{0.01}\right)^{-1} \text{ year}, \quad (8)$$

where $\hat{T}_d = T_d/15$ K and T_d is dust temperature; u_{rad} is the energy density of the radiation field in the region under consideration; $u_{\rm ISRF}$ is the energy density of the standard interstellar radiation field (ISRF), given by Tazaki et al. (2017) as $u_{\rm ISRF} = 8.64 \times 10^{-13}$ erg cm^{-3}; $\bar{\lambda}$ is the mean wavelength of the incident radiation spectrum, γ is radiation field anisotropy, and $|Q_\Gamma|$ is the RAT efficiency. This formulation of $\tau_{rad,p}$ assumes grains to be rotating at the thermal angular velocity, i.e. $\omega \approx \omega_{th}$ (Lazarian & Hoang 2007a).

We again take $\hat{\rho} \sim 1$ and $\hat{s} \sim 1$. We expect $0.1 < \gamma \leq 1$, as $\gamma \sim 0.1$ in the diffuse ISM (Draine & Weingartner 1996), and $\gamma \lesssim 1$ in the immediate vicinity of a protostar (Tazaki et al. 2017). As we

Table 3. A summary of the time-scales which we estimate in the Anomalous Region/Fork. Note that $a_{-5} = (a/10^{-5}\,\mathrm{cm})$; $a_{-5} = 1$ indicates grain size $a = 0.1\,\mu\mathrm{m}$.

Mechanism	Characteristic Time-scale	Time-scale value (years)	Dominant grain size regime (μm)
B-RATs	τ_{Lar}	$\sim 1.6(10^{-5} - 10^{-3})\,a_{-5}^{2}$	$\lesssim 0.005{-}0.1$
k-RATs	$\tau_{rad,\,p}$	$\lesssim 1.7 \times 10^{-5}\,a_{-5}^{\frac{1}{2}}$	$\gtrsim 0.005{-}0.1$
v-MATs	τ_{mech}	$\gtrsim 72(\omega/\omega_{th})$	—
Randomization	τ_{gas}	$\sim 0.017 - 1.7\,a_{-5}$	—

are specifically considering the radiation field from Source I, which we expect to be strongly anisotropic, we take $\gamma \sim 1$. Note that this implies that radiation from Source I is effectively unobscured in the western arm of the Fork; a justifiable assumption if the polarized emission indeed arises from the Source I outflow cavity wall, which we discuss further below. We further take $|Q_\Gamma| \leq 0.4$ (Lazarian & Hoang 2007a; Tazaki et al. 2017), and so $\gamma|Q_\Gamma|/0.01 \lesssim 40$.

The luminosity of Source I is not well characterized, but is thought to be $>10^4\,\mathrm{L}_\odot$ (Menten & Reid 1995). The plane-of sky separation between the Fork and Source I is $\sim 3.5''$, which at a distance of 388 pc corresponds to $\sim 2 \times 10^{16}$ cm ($\sim$1400 au). We thus estimate the radiation energy density in the vicinity of the fork to be

$$u_{rad} = \frac{L}{4\pi R^2 c} > 2.7 \times 10^{-7}\,\mathrm{erg\,cm^{-3}}, \tag{9}$$

where L is the luminosity of Source I and R is the separation between Source I and the Fork.

The effective brightness temperature of Source I is $\sim$1500 K (Reid et al. 2007), and so from Wien's Law, we infer a peak emission wavelength of photons emanating from Source I of $\sim 1.9\,\mu$m. We thus take $\bar{\lambda}/1.2\mu\mathrm{m} \sim 1.6$. We note that as with taking $\gamma \sim 1$, this assumes that emission from Source I is unobscured in the Fork. We discuss this assumption further below.

Dust temperature T_d can be estimated for silicates using the relation

$$T_d \approx 16.4 \left(\frac{u_{rad}}{u_{\mathrm{ISRF}}}\right)^{\frac{1}{6}}\,\mathrm{K} \tag{10}$$

(Draine 2011). Using our value of u_{rad} from equation (9), we estimate $T_d \approx 135$ K in the Fork, and so $\hat{T}_d^{\frac{1}{2}} \approx 3$.

Combining these estimates, equation (8) becomes

$$\tau_{rad,\,p} \lesssim 1.7 \times 10^{-5}\,a_{-5}^{\frac{1}{2}}\ \mathrm{year}. \tag{11}$$

Comparing this to the Larmor time-scale in the Fork, as given in equation (5), we find the condition for k-RATs to dominate over B-RATs, $\tau_{rad,\,p} < \tau_{Lar}$, is equivalent to

$$a_{-5} > 0.05 - 1.0, \tag{12}$$

or equivalently,

$$a > 0.005 - 0.1\,\mu\mathrm{m}. \tag{13}$$

This suggests that in the vicinity of Source I, $\tau_{rad,\,p} < \tau_{Lar}$ will hold for larger paramagnetic dust grains if Source I remains relatively unobscured, and so we can plausibly expect to see a polarization pattern arising from k-RATs.

While highly uncertain, the minimum values of a for which $\tau_{rad,\,p} < \tau_{Lar}$ that we find are plausible grain sizes in a dense molecular cloud (e.g. Draine & Li 2007). The maximum grain size in the diffuse ISM is $0.25 - 0.3\,\mu$m (Mathis, Rumpl & Nordsieck 1977; Draine & Li 2007), indicating that while k-RATs could potentially dominate over B-RATs in the vicinity of Source I even in relatively pristine ISM material, the grain growth which is likely to have occurred in such a dense environment (Ysard et al. 2013) makes $\tau_{rad,\,p} < \tau_{Lar}$ more likely to hold. Moreover, if grains are indeed aligned by k-RATs downstream of the shocks associated with BN/KL ejecta and/or the expansion of the Source I outflow, it suggests that these shocks have not destroyed all of the larger dust grains in the cloud.

3.2.10 *Gas damping time-scale*

A further requirement for grains to precess around any given axis is that the precession time-scale around that axis is shorter than the gas damping time-scale τ_{gas}, the characteristic time-scale of grain randomization by gas collisions (Lazarian & Hoang 2007a). The highly ordered polarization geometry of the Fork – and across OMC-1 – strongly suggests that the dust grains are not randomized. However, as a check on our previous analysis, we estimate the gas damping time-scale in the Fork.

Hoang & Lazarian (2016) give τ_{gas} as

$$\tau_{gas} = 6.6 \times 10^4\,\hat{\rho}\hat{s}^{-\frac{2}{3}}a_{-5}\Gamma_{\parallel}^{-1}\left(\frac{300\,\mathrm{K}^{\frac{1}{2}}\mathrm{cm}^{-3}}{T_{gas}^{\frac{1}{2}}n_{\mathrm{H}}}\right)\ \mathrm{year}, \tag{14}$$

where $\Gamma_{\parallel}$ is a factor of order unity characterizing grain geometry and T_{gas} is gas temperature. We take $\Gamma_{\parallel} \sim 1$, continue to take $\hat{s} \sim 1$ and $\hat{\rho} \sim 1$ and $n_{\mathrm{H}} \sim 10^6 - 10^8\,\mathrm{cm}^{-3}$ (cf. Section 3.2.3), and assume $T_{gas} \sim T_{dust} \approx 135$ K. Equation (14) thus becomes

$$\tau_{gas} \sim 0.017 - 1.7\,a_{-5}\ \mathrm{year}. \tag{15}$$

Comparison of equation (15) with equations (5) and (11) shows that there is no value of a_{-5} at which τ_{gas} is the shortest time-scale. $\tau_{gas} < \tau_{rad,\,p}$ holds only for unphysically small grains, with $a_{-5} < 10^{-10}$, at which size $\tau_{Lar} \ll \tau_{gas}$ would hold if such grains existed. Conversely, $\tau_{gas} < \tau_{Lar}$ only for unphysically large grains, with $a_{-5} > 10^3 - 10^5$, at which size $\tau_{rad,\,p} \ll \tau_{gas}$. These time-scales are summarized in Table 3 and illustrated in Fig. 9. For the values of τ_{Lar} and $\tau_{rad,\,p}$ which we find in the Fork, τ_{gas} would need to be smaller by at least three to five orders of magnitude for a regime to exist in which it is the shortest time-scale. Thus grains in the Fork cannot have their alignments randomized by gas collisions faster than they can be induced to precess around either the magnetic field direction or the radiation anisotropy gradient by RATs.

3.2.11 *Discussion of grain alignment in the Anomalous Region/Fork*

In the preceding analysis, by taking $\gamma \sim 1$ and $\bar{\lambda} = 1.9\,\mu$m we have assumed that the polarized emission arises in a location where there is minimal obscuration of Source I. Such obscuration would introduce absorption, re-emission, and scattering of radiation, reducing the

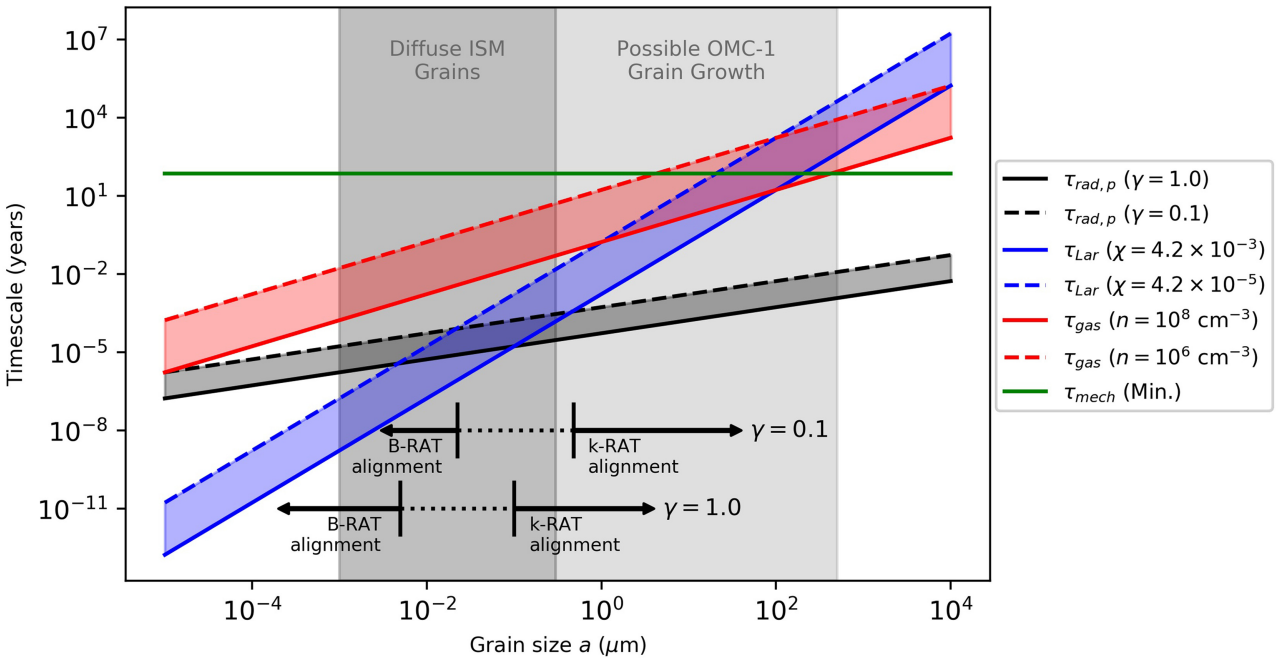

Figure 9. A comparison of the radiative precession ($\tau_{rad,p}$), Larmor (τ_{Lar}), gas damping (τ_{gas}), and mechanical alignment (τ_{mech}) time-scales which we estimate in the western arm of the Anomalous Region/Fork, as a function of grain size a. Note that the shortest time-scale determines the precession axis; thus, small grains are likely to be aligned by B-RATs to precess around the magnetic field direction, and large grains are likely to be aligned by k-RATs to precess around the radiation anisotropy vector. The minimum value of τ_{mech} which we show assumes $\omega \approx \omega_{th}$, i.e. that grains are rotating at the thermal angular velocity. Other time-scales are shown at their fastest and slowest likely values as determined by the dominant quantifiable source of uncertainty in their determination, as discussed in the text, with their likely range shaded. The dark grey shaded region marks the grain size distribution in the diffuse ISM (Draine & Li 2007); the light grey shaded area shows the maximum extent of grain growth likely in OMC-1 ($a_{max} < 500$ μm; see Section 3.1), although we note that grains larger than a few microns are unlikely to be found outside of the Source I disc.

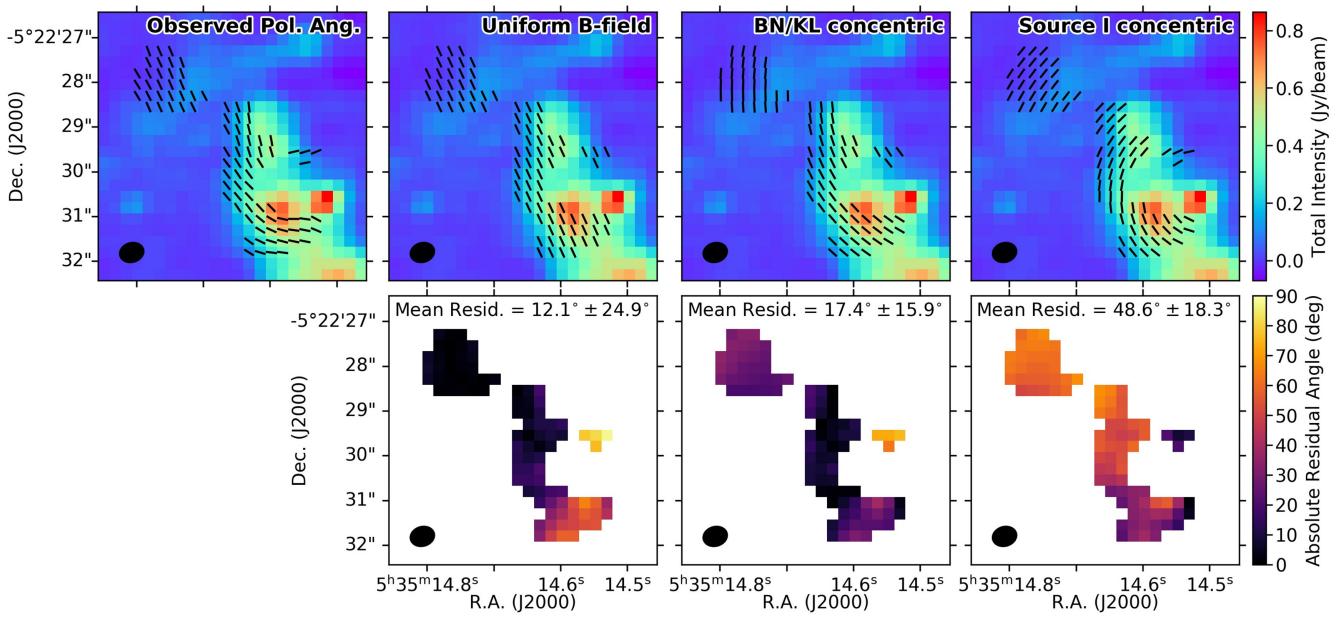

Figure 10. Comparison of models in the Ridge. Top row shows observed and model polarization geometries, plotted on Stokes *I* emission, bottom row shows absolute difference in angle between data and models. Far left: Observed polarization vectors. Centre left: polarization vectors aligned 26° E of N, perpendicular to the large-scale magnetic field direction (hypothesized alignment mechanism: B-RATs). Centre right: polarization vectors concentric around the BN/KL explosion centre (hypothesized alignment mechanism: B-RATs/v-MATs). Far right: polarization vectors concentric around Source I (hypothesized alignment mechanism: k-RATs). All maps are shown on 0.25″ (approximately Nyquist-sampled) pixels. The synthesized beam size is shown in the lower left-hand corner of each plot.

anisotropy γ in the radiation field and increasing $\bar{\lambda}$, and so increasing $\tau_{rad,\,p}$. If $\gamma < 1$ but remains above the value in the diffuse ISM, the minimum grain size alignable by k-RATs would increase by a factor of up to 4.8, as shown in Fig. 9, for $\bar{\lambda} = 1.9\,\mu$m.

The peak column density in emission potentially associated with the Fork is $N_{\rm H_2} = 3.1 \times 10^{24}\,{\rm cm}^{-2}$, as measured at the methyl formate peak MF2 (Favre et al. 2011). Taking $N_H \sim 2.2 \times 10^{21}\,{\rm cm}^2 A_V$ (Güver & Özel 2009) and $A_K/A_V = 0.112$ (Rieke & Lebofsky 1985), this implies a maximum K-band extinction $A_K \sim 300$ (the K band is centred on 2.2 μm, very similar to our value of $\bar{\lambda}$). This suggests that strongly directional mid-infrared emission from Source I will drop off very rapidly as it encounters the high-density ambient medium of OMC-1. The brightness of the submillimetre thermal emission from the Fork which we observe also suggests re-radiation of a significant number of photons. This strongly suggests that if the polarized emission which we observe in the western arm of the Fork does indeed arise from grains aligned by k-RATs, the polarized emission must arise from the cavity wall of the Source I outflow, where the radiation field of Source I may remain largely unobscured.

There are a number of reasons why the k-RAT mechanism might be important to some depth into the western arm of the Fork despite the rapid increase in $\tau_{rad,\,p}$ with increasing extinction. Firstly, longer-wavelength photons could maintain a sufficiently short value of τ_{rad} to permit k-RAT alignment: for our slower value of τ_{Lar}, $\tau_{rad,\,p}$ as given in equation 11 could be increased by a factor ∼480 and remain the shorter time-scale at $a = 0.3\,\mu$m, suggesting that k-RATs could potentially remain significant even for values of $\bar{\lambda}$ in the submillimetre regime. Additionally, our value of τ_{Lar} is a lower limit, as $B \sim 10\,\mu$G is an upper limit (Cortes et al. 2021), unless super-paramagnetic inclusions are resorted to to increase χ. Similarly, $\tau_{rad,\,p}$ is an upper limit, as $L = 10^4\,{\rm L}_\odot$ is a lower limit on the luminosity of Source I (Menten & Reid 1995). Finally, our KS tests suggest that the dispersion of Q and U values is systematically lower in the western arm of the Fork than elsewhere in OMC-1; this suggests some difference either in alignment mechanism or in non-thermal velocity dispersion in this region, either or both of which could arise if the emission does indeed arise from the Source I outflow cavity wall rather than the ambient medium.

If grains in the western arm of the Fork remain aligned by B-RATs, a large-scale reorientation of the magnetic field must have taken place in the region, away from either the large-scale field direction or the radial field around the BN/KL outflow that we see in the eastern arm. Cortes et al. (2021) find a magnetic Reynolds number $R_m = 1.7 \times 10^5 \gg 1$ in OMC-1, indicating that the magnetic field is well coupled to the gas. If the field has indeed been reordered in this region, its orientation is suggestive of ordered infall or outflow of material. If the material were infalling on to the Ridge/Hot Core region, this would be similar to the behaviour seen on much larger size scales in hub-filament systems (e.g. Pillai et al. 2020), where magnetic fields are seen to run along filaments of material infalling on to the central hub. The reordered field representing outflowing material is more difficult to physically motivate, as the most likely cause of such a gas outflow would be the BN/KL explosion, with which our observed polarization geometry is not consistent.

This analysis, summarized in Tables 2 and 3, and illustrated in Fig. 9, suggests that it may be possible for moderately large grains in the vicinity of extremely luminous sources such as Source I to be aligned by k-RATs rather than by B-RATs, provided that the source remains relatively unobscured. However, it also suggests that the efficiency of k-RAT alignment will drop off very quickly with distance from Source I due to the high mid-infrared optical depth of the ambient medium of OMC-1. We emphasize that our estimates of both $\tau_{rad,\,p}$ and τ_{Lar} are highly uncertain. We do not have enough information to definitively identify grains in the Fork as being aligned either by k-RATs or by B-RATs.

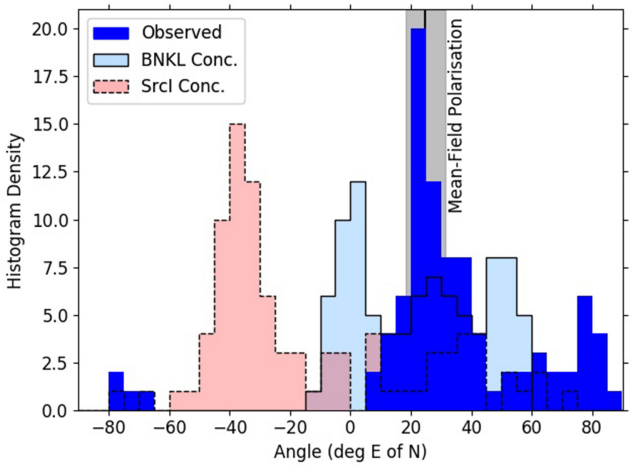

Figure 11. Histogram of polarization angles in the Ridge (blue), compared with models: polarization vectors concentric around (1) the centre of the BN/KL explosion (light blue, solid outline), (2) Source I (red, dashed outline). The polarization angle associated with the mean 116-degree magnetic field direction is marked. Angles are measured on 0.25″ (approximately Nyquist-sampled) pixels.

3.3 Main Ridge

The main Ridge of OMC-1 (hereafter 'the Ridge') is an active site of ongoing star formation, an elongated structure which contains a number of dense cores (e.g. Hirota et al. 2015). Most famous amongst these is the Hot Core (Ho et al. 1979), a dense but apparently externally heated and starless structure (Zapata, Schmid-Burgk & Menten 2011) separated from Source I by ∼1″.

The polarization pattern in the Ridge is strongly peaked on the 26° E of N polarization direction perpendicular to the large-scale magnetic field, as shown in Fig. 11, with deviations in the Hot Core, and on a position NE of Source I and disconnected from the main body of the Ridge, which we tentatively associate with the Source I outflow. KS and Kuiper tests, performed as described in Section 3.2.1, show that, away from the Hot Core and the Source I outflow, the observed polarization pattern is consistent ($p > 0.05$) with that corresponding to the large-scale magnetic field for angular dispersion values in the range $4^\circ \lesssim \sigma_\theta \lesssim 20^\circ$ (KS test), or $5^\circ \lesssim \sigma_\theta \lesssim 16^\circ$ (Kuiper test), as shown in Fig. 12. The best agreement with the data is at $\sigma_\theta = 8^\circ$, matching the equivalent value in the eastern arm of the Fork.

There is no angular dispersion value at which the polarization pattern in the Ridge is consistent with being concentric around either the centre of the BN/KL explosion or around Source I, suggesting that the grains remain aligned by B-RATs to be perpendicular to the large-scale magnetic field. The polarization vectors in the Ridge, rotated by 90° to trace the magnetic field direction, are shown in Fig. 13. We exclude from this figure the vectors tentatively associated with the Source I outflow, as discussed in Section 3.3.1, below. We detect little polarized emission in the Ridge south of the Hot Core; particularly, we do not see polarized emission associated with the source SMA 1 (Beuther et al. 2005), although the Anomalous Region/Fork borders on this source. We similarly detect little polarization on the north-

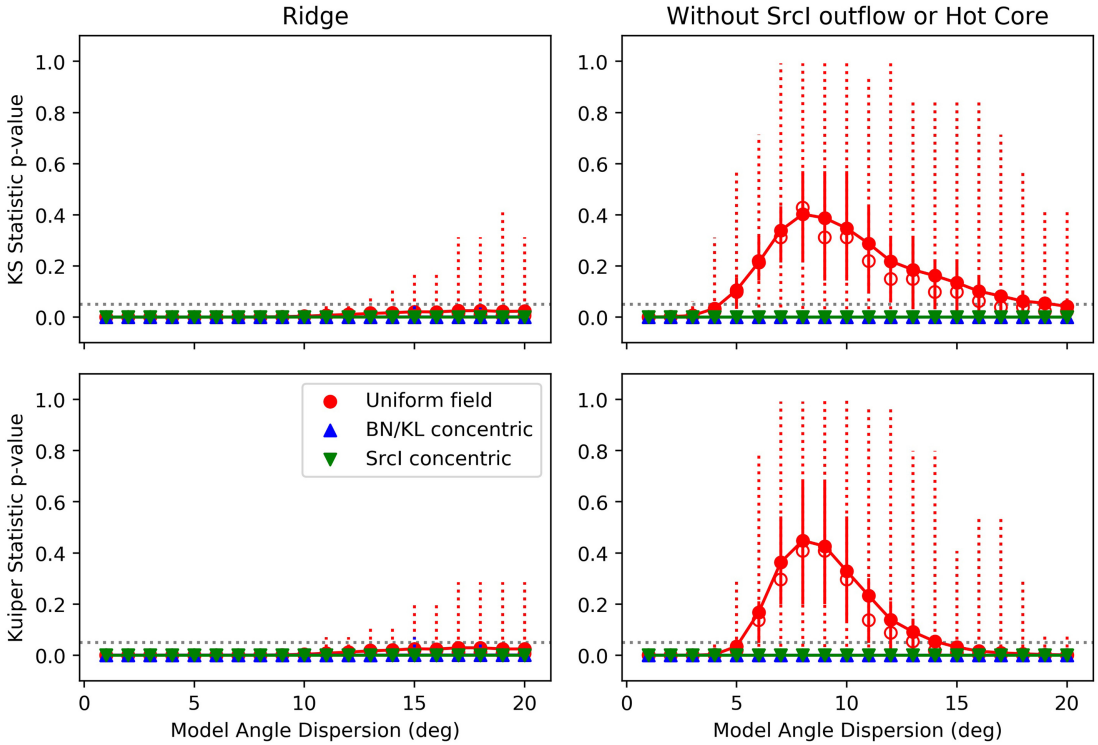

Figure 12. Results of KS and Kuiper tests comparing observed polarization angles in the Ridge to a set of Monte Carlo realizations of our three models with specified values of dispersion in polarization angle. Description of panels as in Fig. 8.

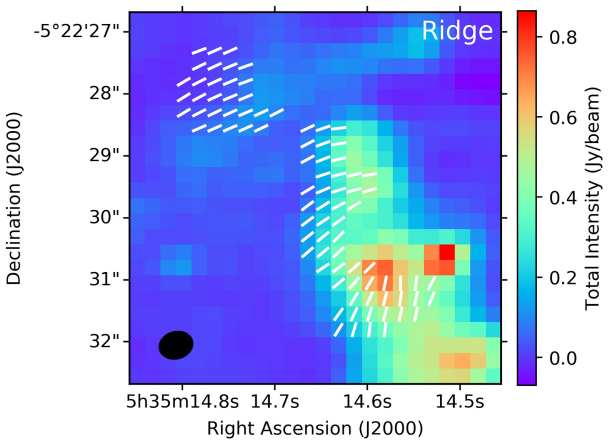

Figure 13. Magnetic field vectors in the Ridge, obtained by rotating the polarization vectors by 90°, on the assumption that grains are aligned by B-RATs. We exclude the vectors tentatively associated with emission from the Source I outflow.

western side of the Ridge. A possible explanation for this is a lack of a dominant polarization mechanism in these regions.

Where polarized emission is detected in the Ridge, its direction is consistent with that predicted if the large-scale magnetic field direction persists to the highest-density and smallest-scale structures in OMC-1. If the magnetic field direction is indeed consistent over orders of magnitude in size scale, it might suggest that the field remains dynamically important at the highest densities. On larger scales in molecular clouds, magnetic fields are consistently found to be perpendicular to filamentary structures where (a) the filament is gravitationally unstable and (b) the magnetic field is, on scales larger than the filament, dynamically important (Soler et al. 2013; Planck Collaboration 2016). Although the Ridge is not a filament in the usual sense, it does meet these conditions. However, Cortes et al. (2021) find that the energy in the magnetic field is ∼3 orders of magnitude less than the maximum energy in the explosive outflow, and $R_m = 1.7 \times 10^5 \gg 1$, indicating that the field moves with the gas, and so argue that the magnetic field in OMC-1 has been reordered as it moves with the outflowing gas to be radial around the BN/KL explosion. Our results suggest that this reordering may not have taken place in the vicinity of the Ridge. The major axis of the Ridge is approximately parallel to the BN/KL shock front, and it does not seem to have been disrupted by the BN/KL explosion in the manner of the radial CO streamers that surround OMC-1. It could, however, be the remnant of some larger structure which has been disrupted or ablated by the passage of the BN/KL shock front. This suggests that the field might have retained its original orientation in the vicinity of the Ridge not because of its own energetic importance, but rather because of the ability of the gas in the Ridge to which it is coupled to resist disruption by the effects of the BN/KL explosion.

The polarization pattern in the Hot Core is broadly similar to that the rest of the Ridge, with some deviation on the south-western side of the core. This deviation, although not well-resolved, is somewhat suggestive of the pinched field predicted for strongly magnetized dense cores. A dynamically important magnetic field is broadly expected to support a prestellar core against, and to impose a preferred direction on, gravitational collapse (Mouschovias 1976), producing the classical 'hourglass' magnetic field indicative of ambipolar-diffusion-mediated gravitational collapse (e.g. Fiedler & Mouschovias 1993). However, it is not clear why such an hourglass morphology would only be apparent on one side of the core, or whether the energetic importance of the magnetic field in the region

is sufficiently high to allow such collapse to occur (Cortes et al. 2021). Higher-resolution polarization observations are required in order to understand the role of magnetic fields in the evolution of the Hot Core.

We note for completeness that in the south-west side of the Hot Core, the polarization vectors are also consistent with being elliptical around Source I, with $e \gtrsim 0.9$, as would be expected for k-RAT alignment concentric around Source I in material displaced along the line of sight with respect to Source I. This is the only region in the Ridge where polarization vectors are consistent with k-RAT alignment. However, as argued below, it appears unlikely that k-RATs can dominate over B-RATs in the Ridge, and there is no clear reason for the Hot Core to be the exception to this.

3.3.1 Source I outflow?

Polarization is detected at a position north-east of Source I, and disconnected from the Ridge. This region, labelled as 'Source I outflow?' in Fig. 2, has polarization vectors approximately perpendicular to those in both the Ridge and Source I, and thus are inconsistent both with the 26° E of N polarization direction perpendicular to the large-scale field direction and with being concentric around the BN/KL explosion, as can be seen in Fig. 10. These vectors have orientations qualitatively similar to the SiO polarization vectors detected by Hirota et al. (2020) in the north-eastern lobe of the Source I outflow, perhaps suggesting that this polarized emission arises from dust in the outflow cavity walls, as is hypothesized for the Fork (Wright & Plambeck 2017), or entrained by the outflow. We note, however, that the size scale of the SiO measurements is quite different to our observations (Hirota et al. (2020) observed $\sim 1''$ around Source I), and so assigning this emission to the Source I outflow is speculative.

If the dust grains in the outflow are aligned by B-RATs, they could be tracing a helical magnetic field structure (Hirota et al. 2020). However, the vector orientations are also qualitatively similar to being concentric around Source I, as shown in Fig. 10. This might suggest that grains in this region could instead be aligned by k-RATs, as we hypothesize in the Anomalous Region/Fork. It seems plausible that the extreme conditions apparently giving rise to k-RATs in the Fork to the south-east of Source I might also be expected to arise in the north-western outflow cone; however, we do not have sufficient evidence to conclusively determine the grain alignment mechanism in this region.

3.3.2 B-RAT versus k-RAT alignment in the Ridge

With the exception of the handful of vectors tentatively associated with the Source I outflow, the polarization pattern in the Ridge is inconsistent with being induced by k-RATs driven by Source I. Given that the Ridge is at a similar or smaller distance to Source I than is the Anomalous Region/Fork, this raises the question of how its grains have apparently retained their original alignment with respect to the magnetic field.

The requirement for k-RATs to dominate over B-RATs is $\tau_{rad,\,p} < \tau_{Lar}$. The material of the Ridge has a higher column density ($N_{\rm H_2} = 5.4 \times 10^{24}\,{\rm cm^{-2}}$; Favre et al. 2011) than its surroundings, corresponding to a peak K-band extinction $A_K \sim 500$. For much of the Ridge, the emission from Source I will be further obscured by its disc. The effect of this obscuration will be to increase $\bar{\lambda}$ and decrease γ, thereby increasing $\tau_{rad,\,p}$, as discussed in Section 3.2.11. We note also that the polarized emission which we see in the Ridge mostly arises from its eastern side, away from Source I. The hypothesized k-RAT alignment in the Fork appears to depend on unobscured emission from Source I driving alignment in the outflow cavity walls. This effect is less likely to apply in the Ridge, although the northern part of the Ridge could be impacted on by the Source I outflow, depending on the relative orientations of the Ridge and the outflow.

We also expect τ_{Lar} to decrease in high-density material, as magnetic field strength B is expected to scale with density such that $B \propto n^{0.5}$ or $B \propto n^{0.66}$ (e.g. Crutcher 2012).

While these two effects are difficult to quantify, the polarization geometry which we observe on the eastern side of the Ridge suggests that between them they are sufficient to result in $\tau_{rad,\,p} > \tau_{Lar}$, allowing B-RATs to dominate over k-RATs, despite the proximity of Source I. This again suggests that k-RAT alignment, if present in ISM material, is restricted to the immediate vicinity of (proto)stars, and in the vast majority of ISM environments, grains will remain aligned relative to the magnetic field.

We note that the increase in density will also decrease τ_{gas} as shown in equation (14), although this will be mitigated by a decrease in T_{gas} as the radiation field of Source I is increasingly obscured (cf. equation 10). None the less, as discussed in Section 3.2.10, a density increase of several orders of magnitude would be required to make $\tau_{gas} < \tau_{Lar}$ hold for physically plausible grain sizes, particularly if τ_{Lar} is itself shortened in the Ridge.

3.4 MF4/MF5

Polarization vectors in MF4 and MF5 (Favre et al. 2011; collectively known as the Northwest Clump) are qualitatively similar both to the pattern predicted for alignment perpendicular to the large-scale field direction, and to that for being concentric around the BN/KL outflow centre or Source I. The two clumps are at a similar distance to the BN/KL explosion centre as is the Ridge, and have complex substructure, with each consisting of three distinct velocity components (Pagani et al. 2017). We detect only six independent beams over MF4/MF5.

As shown in Figs 14 and 15, the polarization pattern in MF4/MF5 is more consistent with that expected for concentric polarization around BN/KL than with the mean field direction or with being concentric around Source I. This is confirmed by KS and Kuiper tests, performed as described in Section 3.2.1, which show that only the BN/KL-concentric model can be made consistent ($p > 0.05$) with the data, as shown in Fig. 16. A wide range of angular dispersion values, $\sigma_\theta \gtrsim 4.5°$ (KS test) or $2.5° \lesssim \sigma_\theta \lesssim 17.5°$ (Kuiper test), produce patterns consistent with the small sample of observed vectors, but the best agreement is found at $\sigma_\theta \sim 8°$, matching the equivalent values in the eastern arm of the Fork and the Ridge. Our results thus support the interpretation of Cortes et al. (2021) that in this region, the magnetic field has been realigned by the effects of the BN/KL explosion. The magnetic field implied by our polarization observations is shown in Fig. 17.

3.5 Compact Ridge/MF1

The Compact Ridge (also known as MF1) is a $\sim 4.3\,{\rm M_\odot}$ clump (Favre et al. 2011), found by Pagani et al. (2017) to have extremely narrow ($\sim 1\,{\rm km\,s^{-1}}$) linewidths. Pagani et al. (2017) thus suggest that MF1 appears not to have yet to have been affected by the BN/KL explosion, and so place it at least 10 000 AU, and likely $\sim$ 20 000 AU, either in front of or behind the explosion centre along the line of sight. It is thus unlikely to be physically associated with the other dense clumps that we observe.

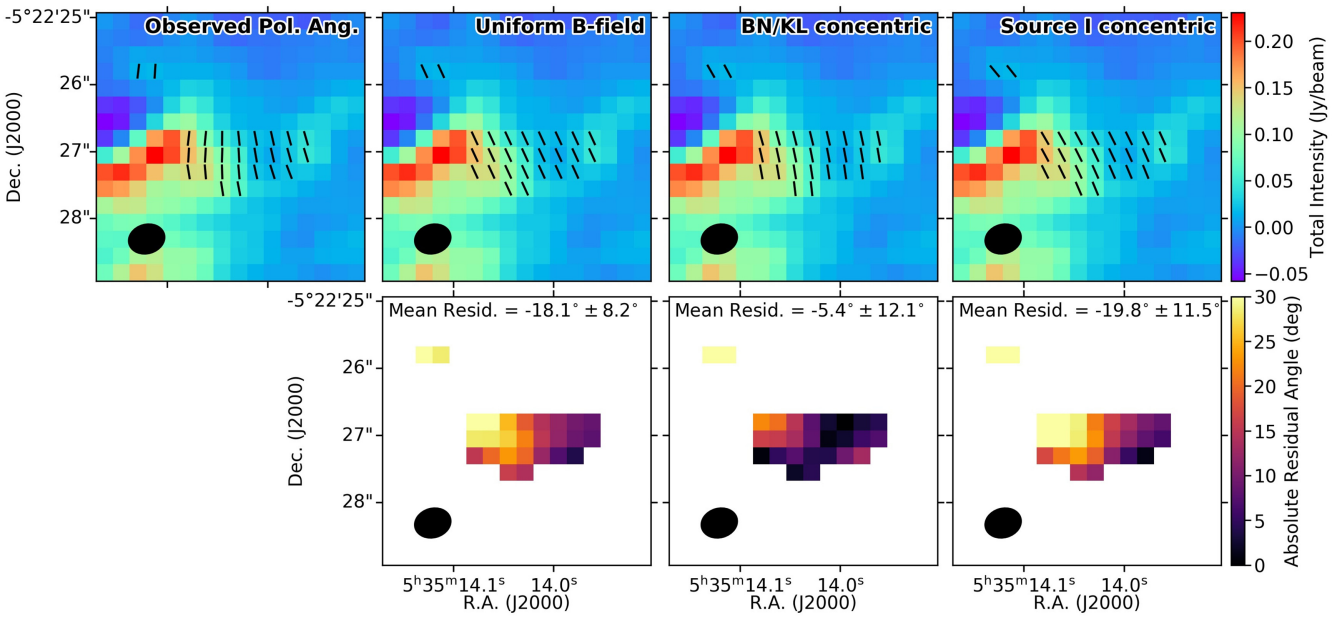

Figure 14. Comparison of models in MF4/MF5. Top row shows observed and model polarization geometries, plotted on Stokes *I* emission, bottom row shows absolute difference in angle between data and models. Far left: Observed polarization vectors. Centre left: polarization vectors aligned 26° E of N, perpendicular to the the large-scale magnetic field direction (hypothesized alignment mechanism: B-RATs). Centre right: polarization vectors concentric around the BN/KL explosion centre (hypothesized alignment mechanism: B-RATs/v-MATs). Far right: polarization vectors concentric around Source I (hypothesized alignment mechanism: k-RATs). In the bottom row, the colour table saturates at a difference in angle of 30°, to emphasize the differences between the models. All maps are shown on 0.25″ (approximately Nyquist-sampled) pixels. The synthesized beam size is shown in the lower left-hand corner of each plot.

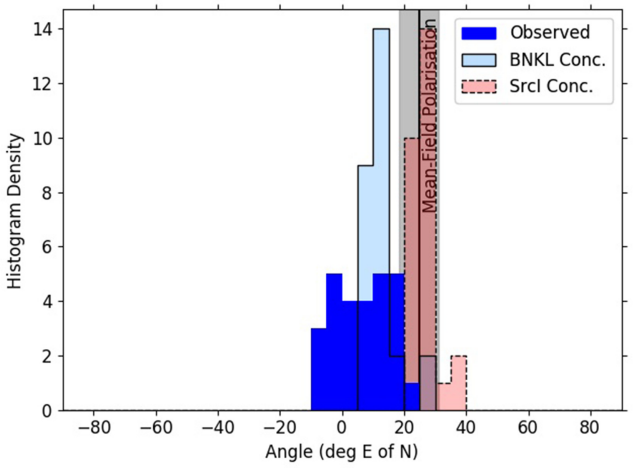

Figure 15. Histogram of polarization angles in the MF4/MF5 (blue), compared with models: polarization vectors concentric around (1) the centre of the BN/KL explosion (light blue, solid outline), (2) Source I (red, dashed outline). The polarization angle associated with the mean 116-degree magnetic field direction is marked. Angles are measured on 0.25″ (approximately Nyquist-sampled) pixels.

The polarization pattern in MF1 is inconsistent with being concentric around either BN/KL or Source I, and broadly similar to the polarization pattern expected for grains aligned perpendicular to the large-scale 116-degree field, as shown in Figs 18 and 19. This result is in keeping with the hypothesis that the region is at a significant distance from the other clumps considered here. We can with some reliability in MF1 expect grains to remain aligned by B-RATs, and so we show the polarization vectors, rotated by 90° to trace the magnetic field direction, in Fig. 20. However, KS

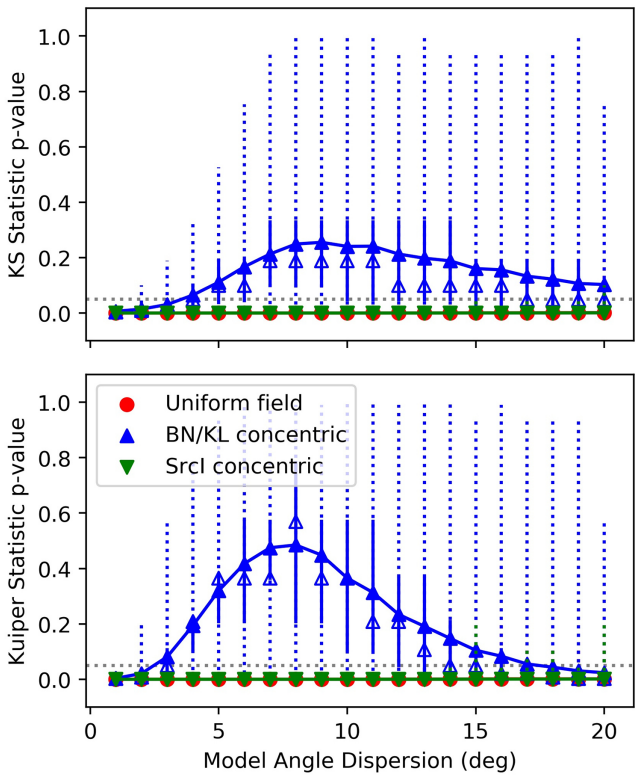

Figure 16. Results of KS and Kuiper tests comparing observed polarization angles in MF4/MF5 to a set of Monte Carlo realizations of our three models with specified values of dispersion in polarization angle. Description of panels as in Fig. 8.

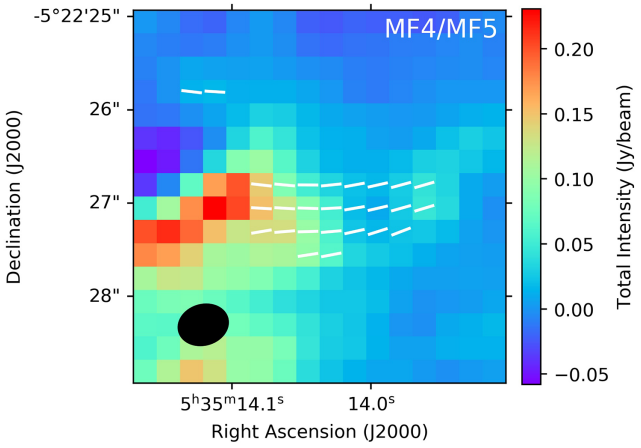

Figure 17. Magnetic field vectors in MF4/MF5, obtained by rotating the polarization vectors by 90°.

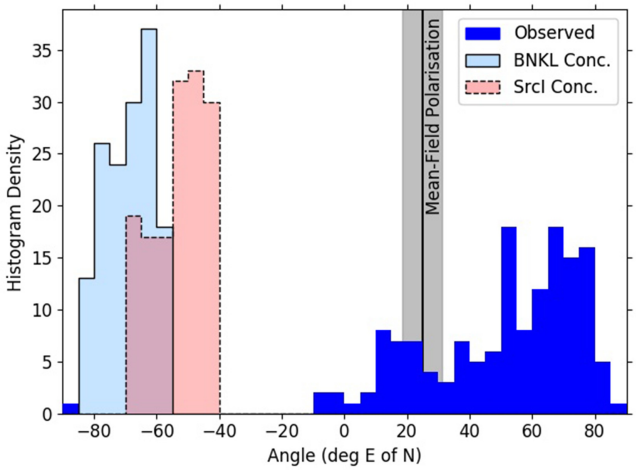

Figure 19. Histogram of polarization angles in MF1 (blue), compared with models: polarization vectors concentric around (1) the centre of the BN/KL explosion (light blue, solid outline), (2) Source I (red, dashed outline). The polarization angle associated with the mean 116-degree magnetic field direction is marked. Angles are measured on 0.25″ (approximately Nyquist-sampled) pixels.

and Kuiper tests, performed as described in Section 3.2.1, show that none of our proposed simple models can be made consistent with the observed polarization pattern. We do not show the results of these tests in a figure, as in every case $p \ll 0.05$. There is significant ordered variation in the magnetic field direction across MF1, and the implied mean and median magnetic field direction values (147 and 149°, respectively) are similar to, but do not match, the average large-scale field direction. The field lines appear to be bowing away from the mean field direction in the periphery of MF1, turning towards the south (this behaviour is more apparent on the eastern side of the region). A possible interpretation of this behaviour is that the field in MF1 is merging into the large-scale 'hourglass' field morphology observed on larger scales in OMC-1 (Rao et al. 1998; Houde et al. 2004; Pattle et al. 2017). Cortes et al. (2021) also note a transition toward field morphologies matching the large-scale hourglass in the south of OMC-1.

4 SUMMARY

We have presented ALMA Band 7 (881 μm) continuum polarization observations of the centre of the OMC-1 region of the Orion Molecular Cloud.

We divided OMC-1 into five regions: Source I (a massive outflow-driving protostar), the Anomalous Region/Fork, the Main Ridge, MF4/MF5, and the Compact Ridge/MF1. Our key findings are as follows:

(i) In Source I, we found an unresolved polarization geometry parallel to the minor axis of the Source I disc, consistent with polarization arising from dust self-scattering. The Source I disc is

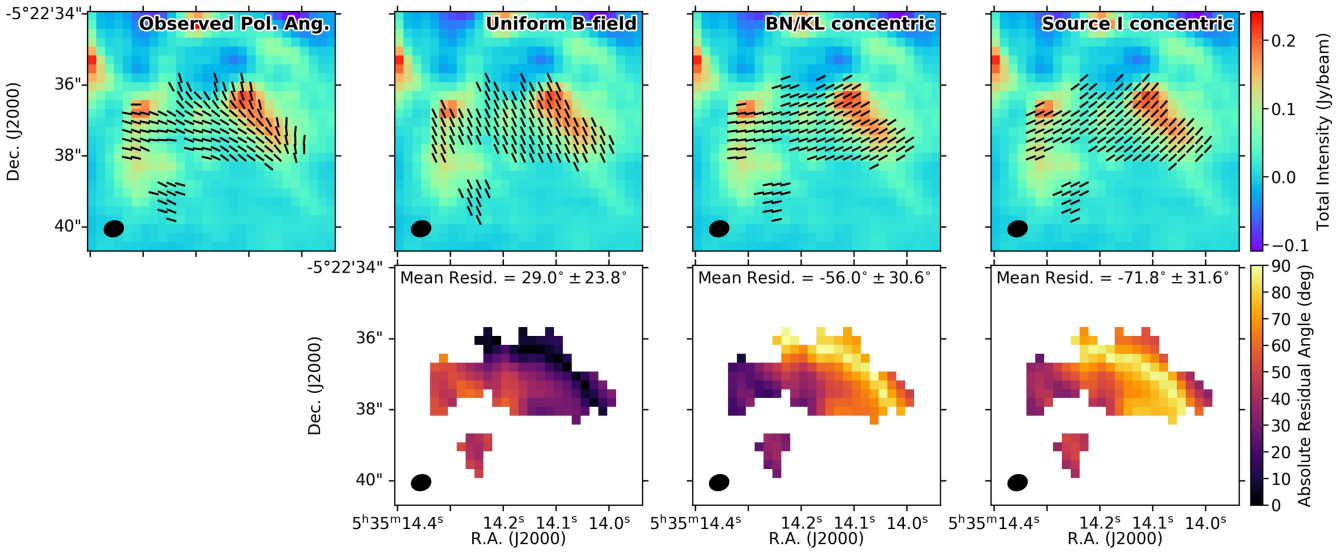

Figure 18. Comparison of models in MF1. Top row shows observed and model polarization geometries, plotted on Stokes *I* emission, bottom row shows absolute difference in angle between data and models. Far left: Observed polarization vectors. Centre left: polarization vectors aligned 26° E of N, perpendicular to the the large-scale magnetic field direction (hypothesized alignment mechanism: B-RATs). Centre right: polarization vectors concentric around the BN/KL explosion centre (hypothesized alignment mechanism: v-MATs). Far right: polarization vectors concentric around Source I (hypothesized alignment mechanism: k-RATs). All maps are shown on 0.25″ (approximately Nyquist-sampled) pixels. The synthesized beam size is shown in the lower left-hand corner of each plot.

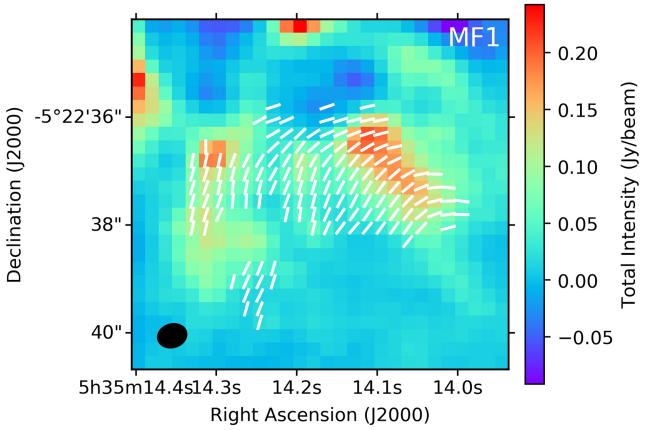

Figure 20. Magnetic field vectors in MF1, obtained by rotating the polarization vectors by 90°.

optically thick and viewed almost edge-on, supporting this interpretation; however, the predicted polarization pattern is degenerate with that for a polarization pattern concentric around the centre of the BN/KL explosion.

(ii) In the eastern arm of the Anomalous Region/Fork, we found a polarization geometry consistent with being concentric around the centre of the BN/KL explosion, consistent with the magnetic field having been reordered to be radial around the BN/KL explosion, as posited by Tang et al. (2010) and Cortes et al. (2021).

(iii) In the western arm of the Fork, a region in which emission may arise from the Source I outflow cavity walls, we found a polarization geometry consistent with being concentric around Source I. We compared the mechanical alignment time-scale τ_{mech} to the Larmor time-scale τ_{Lar} in the Anomalous Region/Fork, finding $\tau_{mech} \gg \tau_{Lar}$, indicating that grains are unlikely to be aligned by subsonic mechanical alignment torques (v-MATs) induced by the passage of shocks associated with the BN/KL explosion or associated with the Source I outflow. We compared the radiative precession time-scale $\tau_{rad,\,p}$ for unobscured emission from Source I to the Larmor time-scale τ_{Lar} in the Anomalous Region/Fork. While our estimates of both time-scales are highly uncertain, we find $\tau_{rad,\,p} < \tau_{Lar}$ for moderately large grains ($> 0.005 - 0.1$ μm), suggesting that grains in this region may be aligned by radiative torques to precess around the radiation anisotropy gradient (k-RATs), i.e. to be perpendicular to the gradient of intensity from Source I. This hypothesis strongly favours the interpretation of emission in the region as arising from the Source I outflow cavity walls, as Source I must remain relatively unobscured for k-RATs to dominate in this manner. Alternatively, the grains may continue to precess around the magnetic field direction (B-RATs), and so could trace infall of material on to the Main Ridge/Hot Core region.

(iv) In the Main Ridge, we found a polarization geometry consistent with that of the large-scale magnetic field in the region, and so determined that grains are aligned perpendicular to the magnetic field (B-RAT alignment). The consistency with the large-scale magnetic field, despite recent findings that the magnetic field is energetically subdominant compared to the BN/KL outflow, may result from the field being well coupled to gas in the Ridge that has not been disrupted by the BN/KL explosion. We identified an area of polarized emission north-east of Source I possibly arising from the Source I outflow. Grains in this region could trace a helical magnetic field in the outflow or be aligned by k-RATs.

(v) In MF4/MF5, we found a polarization geometry consistent with being concentric around the BN/KL explosion centre, and so tracing a magnetic field that has been reordered to be radial around the BN/KL explosion.

(vi) In the Compact Ridge/MF1, likely located sufficiently far from the BN/KL explosion and Source I to remain uninfluenced by their effects, we found a polarization geometry similar to, but showing ordered deviation from, being perpendicular to the large-scale magnetic field direction. The field may here be merging into the large-scale 'hourglass' field identified in single-dish observations.

Our observation of grains which may be aligned by k-RATs rather than by B-RATs in the vicinity of Source I demonstrates the care which must be taken in the interpretation of polarization observations in extreme environments in the ISM. The complexity of OMC-1, and the similarity between the polarization geometries predicted by our simple models, makes definitively identifying k-RAT alignment difficult. We cannot rule out either k-RAT or B-RAT alignment as having produced the observed polarization geometry. In order to confirm the existence of k-RAT alignment in the vicinity of massive protostars, we will need to observe the polarization geometry around similar sources in other less complex regions.

ACKNOWLEDGEMENTS

We would like to thank the anonymous referee for a helpful report which significantly improved the content of this paper. This paper makes use of the following ALMA data: ADS/JAO.ALMA#2018.1.01162.S. ALMA is a partnership of ESO (representing its member states), NSF (USA) and NINS (Japan), together with NRC (Canada), MOST and ASIAA (Taiwan), and KASI (Republic of Korea), in cooperation with the Republic of Chile. The Joint ALMA Observatory is operated by ESO, AUI/NRAO, and NAOJ. K.P., S.P.L. and Y.W.T. acknowledge support from the Ministry of Science and Technology (MOST), Taiwan, under grant numbers 106-2119-M-007-021-MY3 (K.P., S.P.L.), 109-2112-M-007-010-MY3 (S.P.L.) and 108-2112-M-001-004-MY2 (Y.W.T.). This research was supported in part at the SOFIA Science Center, which is operated by the Universities Space Research Association under contract NNA17BF53C with the National Aeronautics and Space Administration. T.H. acknowledges support by the National Research Foundation of Korea (NRF) grants funded by the Korean government (MSIT) (2019R1A2C1087045). C.W.L. is supported by the Basic Science Research Program through the NRF funded by the Ministry of Education, Science and Technology (NRF-2019R1A2C1010851). This research made use of Astropy, a community-developed core Python package for Astronomy (Astropy Collaboration 2013, 2018), the CASA software suite (McMullin et al. 2007), Starlink software (Currie et al. 2014), currently supported by the East Asian Observatory, and the NASA Astrophysics Data System.

DATA AVAILABILITY

The data used in this paper are available in the ALMA Science Archive (https://almascience.nrao.edu/asax/), under project code 2018.1.01162.S.

REFERENCES

Aizawa M., Suto Y., Oya Y., Ikeda S., Nakazato T., 2020, ApJ, 899, 55
Allen D. A., Burton M. G., 1993, Nature, 363, 54
Andersson B. G., Lazarian A., Vaillancourt J. E., 2015, ARA&A, 53, 501

Andersson B. G., Hoang T., Lopez-Rodriguez E., Vaillancourt J., Sankrit R., Lazarian A., HAWC + Instrument Team, 2018, in American Astronomical Society Meeting Abstracts #231. p. 414.04
Astropy Collaboration, 2013, A&A, 558, A33
Astropy Collaboration, 2018, AJ, 156, 123
Bally J., 2008, Overview of the Orion Complex, ASP Monograph Series. Astronomical Society of the Pacific, San Francisco, California, USA. p. 459
Bally J., Zinnecker H., 2005, AJ, 129, 2281
Bally J., Ginsburg A., Forbrich J., Vargas-González J., 2020, ApJ, 889, 178
Batria W., Wilson T. L., Bastien P., Ruf K., 1983, A&A, 128, 279
Becklin E. E., Neugebauer G., 1967, ApJ, 147, 799
Beuther H. et al., 2005, ApJ, 632, 355
Brauer F., Dullemond C. P., Henning T., 2008, A&A, 480, 859
Chandrasekhar S., Fermi E., 1953, ApJ, 118, 113
Ching T.-C., Lai S.-P., Zhang Q., Yang L., Girart J. M., Rao R., 2016, ApJ, 819, 159
Chrysostomou A., Hough J. H., Burton M. G., Tamura M., 1994, MNRAS, 268, 325
Chuss D. T. et al., 2019, ApJ, 872, 187
Colgan S. W. J., Schultz A. S. B., Kaufman M. J., Erickson E. F., Hollenbach D. J., 2007, ApJ, 671, 536
Cortes P. C. et al., 2016, ApJ, 825, L15
Cortes P. C. et al., 2021, ApJ, 907, 94
Crutcher R. M., 2012, ARA&A, 50, 29
Currie M. J., Berry D. S., Jenness T., Gibb A. G., Bell G. S., Draper P. W., 2014, in Manset N., Forshay P., eds, Astronomical Society of the Pacific Conference Series Vol. 485, Astronomical Data Analysis Software and Systems XXIII. Astronomical Society of the Pacific, San Francisco, California, USA, p. 391
Davis L., 1951, Phys. Rev., 81, 890
Davis L., Greenstein J. L., 1951, ApJ, 114, 206
Dolginov A. Z., Mitrofanov I. G., 1976, Ap&SS, 43, 291
Draine B. T., 1980, ApJ, 241, 1021
Draine B. T., 1996, in Roberge W. G., Whittet D. C. B., eds, Astronomical Society of the Pacific Conference Series Vol. 97, Polarimetry of the Interstellar Medium. Astronomical Society of the Pacific, San Francisco, California, USA, p. 16
Draine B. T., 2011, Physics of the Interstellar and Intergalactic Medium. Princeton University Press, Princeton, New Jersey, USA
Draine B. T., Li A., 2007, ApJ, 657, 810
Draine B. T., Weingartner J. C., 1996, ApJ, 470, 551
Farias J. P., Tan J. C., 2018, A&A, 612, L7
Favre C., Despois D., Brouillet N., Baudry A., Combes F., Guélin M., Wootten A., Wlodarczak G., 2011, A&A, 532, A32
Fiedler R. A., Mouschovias T. C., 1993, ApJ, 415, 680
Giacalone S., Teitler S., Königl A., Krijt S., Ciesla F. J., 2019, ApJ, 882, 33
Ginsburg A., Bally J., Goddi C., Plambeck R., Wright M., 2018, ApJ, 860, 119
Gold T., 1952, MNRAS, 112, 215
Goldreich P., Kylafis N. D., 1982, ApJ, 253, 606
Gómez L., RodrÍguez L. F., Loinard L., Lizano S., Poveda A., Allen C., 2005, ApJ, 635, 1166
Guillet V., Pineau Des Forêts G., Jones A. P., 2007, A&A, 476, 263
Güver T., Özel F., 2009, MNRAS, 400, 2050
Haschick A. D., Baan W. A., 1989, ApJ, 339, 949
Hildebrand R. H., Kirby L., Dotson J. L., Houde M., Vaillancourt J. E., 2009, ApJ, 696, 567
Hirashita H., 2012, MNRAS, 422, 1263
Hirota T., Kim M. K., Kurono Y., Honma M., 2015, ApJ, 801, 82
Hirota T., Machida M. N., Matsushita Y., Motogi K., Matsumoto N., Kim M. K., Burns R. A., Honma M., 2017, Nat. Astron., 1, 0146
Hirota T. et al., 2020, ApJ, 896, 157
Ho P. T. P., Barrett A. H., Myers P. C., Matsakis D. N., Cheung A. L., Chui M. F., Townes C. H., Yngvesson K. S., 1979, ApJ, 234, 912
Hoang T., Lazarian A., 2016, ApJ, 831, 159
Hoang T., Cho J., Lazarian A., 2018, ApJ, 852, 129
Houde M., Dowell C. D., Hildebrand R. H., Dotson J. L., Vaillancourt J. E., Phillips T. G., Peng R., Bastien P., 2004, ApJ, 604, 717
Houde M., Vaillancourt J. E., Hildebrand R. H., Chitsazzadeh S., Kirby L., 2009, ApJ, 706, 1504
Houde M., Hezareh T., Jones S., Rajabi F., 2013, ApJ, 764, 24
Hull C. L. H., Zhang Q., 2019, Front. Astron. Space Sci., 6, 3
Kataoka A. et al., 2015, ApJ, 809, 78
Kataoka A., Okuzumi S., Tazaki R., 2019, ApJ, 874, L6
Kim M. K. et al., 2008, PASJ, 60, 991
Kim M. K., Hirota T., Machida M. N., Matsushita Y., Motogi K., Matsumoto N., Honma M., 2019, ApJ, 872, 64
Kirchschlager F., Bertrang G. H. M., 2020, A&A, 638, A116
Kleinmann D. E., Low F. J., 1967, ApJ, 149, L1
Kounkel M. et al., 2017, ApJ, 834, 142
Kwan J., Scoville N., 1976, ApJ, 210, L39
Kwon W., Looney L. W., Mundy L. G., Chiang H.-F., Kemball A. J., 2009, ApJ, 696, 841
Kwon W., Stephens I. W., Tobin J. J., Looney L. W., Li Z.-Y., van der Tak F. F. S., Crutcher R. M., 2019, ApJ, 879, 25
Lazarian A., Hoang T., 2007a, MNRAS, 378, 910
Lazarian A., Hoang T., 2007b, ApJ, 669, L77
Lazarian A., Hoang T., 2019, ApJ, 883, 122
Luhman K. L., Robberto M., Tan J. C., Andersen M., Giulia Ubeira Gabellini M., Manara C. F., Platais I., Ubeda L., 2017, ApJ, 838, L3
Mathis J. S., Rumpl W., Nordsieck K. H., 1977, ApJ, 217, 425
Matthews L. D., Greenhill L. J., Goddi C., Chand ler C. J., Humphreys E. M. L., Kunz M. W., 2010, ApJ, 708, 80
McKee C. F., Hollenbach D. J., Seab G. C., Tielens A. G. G. M., 1987, ApJ, 318, 674
McMullin J. P., Waters B., Schiebel D., Young W., Golap K., 2007, in Shaw R. A., Hill F., Bell D. J., eds, Astronomical Society of the Pacific Conference Series Vol. 376, Astronomical Data Analysis Software and Systems XVI, p. 127
Menten K. M., Reid M. J., 1995, ApJ, 445, L157
Mouschovias T. C., 1976, ApJ, 207, 141
Ormel C. W., Paszun D., Dominik C., Tielens A. G. G. M., 2009, A&A, 502, 845
Pagani L., Favre C., Goldsmith P. F., Bergin E. A., Snell R., Melnick G., 2017, A&A, 604, A32
Pattle K., Fissel L., 2019, Front. Astron. Space Sci., 6, 15
Pattle K. et al., 2017, ApJ, 846, 122
Pillai T. G. S. et al., 2020, Nat. Astron., 4, 1195
Plambeck R. L., Wright M. C. H., 2016, ApJ, 833, 219
Plambeck R. L. et al., 2009, ApJ, 704, L25
Planck Collaboration et al., 2016, A&A, 586, A138
Rao R., Crutcher R. M., Plambeck R. L., Wright M. C. H., 1998, ApJ, 502, L75
Reid M. J., Menten K. M., Greenhill L. J., Chand ler C. J., 2007, ApJ, 664, 950
Rieke G. H., Lebofsky M. J., 1985, ApJ, 288, 618
Rodríguez L. F., Poveda A., Lizano S., Allen C., 2005, ApJ, 627, L65
Rodríguez L. F., Dzib S. A., Loinard L., Zapata L., Gómez L., Menten K. M., Lizano S., 2017, ApJ, 834, 140
Sadavoy S. I. et al., 2019, ApJS, 245, 2
Sault R. J., Staveley-Smith L., Brouw W. N., 1996, A&AS, 120, 375
Schleuning D. A., 1998, ApJ, 493, 811
Simpson J. P., Colgan S. W. J., Erickson E. F., Burton M. G., Schultz A. S. B., 2006, ApJ, 642, 339
Soler J. D., Hennebelle P., Martin P. G., Miville-Deschênes M. A., Netterfield C. B., Fissel L. M., 2013, ApJ, 774, 128
Tang Y.-W., Ho P. T. P., Koch P. M., Rao R., 2010, ApJ, 717, 1262
Tazaki R., Lazarian A., Nomura H., 2017, ApJ, 839, 56
Ward-Thompson D. et al., 2017, ApJ, 842, 66
Wardle M., 1998, MNRAS, 298, 507
Wright M. C. H., Plambeck R. L., 2017, ApJ, 843, 83
Wright M., Plambeck R., Hirota T., Ginsburg A., McGuire B., Bally J., Goddi C., 2020, ApJ, 889, 155
Ysard N. et al., 2013, A&A, 559, A133

Zapata L. A., Schmid-Burgk J., Ho P. T. P., Rodríguez L. F., Menten K. M., 2009, ApJ, 704, L45
Zapata L. A., Schmid-Burgk J., Menten K. M., 2011, A&A, 529, A24

[1]*Centre for Astronomy, Department of Physics, National University of Ireland Galway, University Road, Galway H91 TK33, Ireland*
[2]*Institute of Astronomy, Department of Physics, National Tsing Hua University, No. 101, Section 2 Guangfu Road, Hsinchu 30013, Taiwan*
[3]*Academia Sinica Institute of Astronomy and Astrophysics, No. 1, Section 4 Roosevelt Road, Taipei 10617, Taiwan*
[4]*Radio Astronomy Lab, University of California, 501 Campbell Hall, Berkeley CA 94720-3441, USA*
[5]*SOFIA Science Center, Universities Space Research Association, NASA Ames Research Center, Moffett Field, CA 94035, USA*
[6]*Korea Astronomy and Space Science Institute, 776 Daedeokdae-ro, Yuseong-gu, Daejeon 34055, Republic of Korea*
[7]*Centre de recherche en astrophysique du Québec & département de physique, Université de Montréal, C.P. 6128 Succ. Centre-ville, Montréal, QC, H3C 3J7, Canada*
[8]*CAS Key Laboratory of FAST, National Astronomical Observatories, Chinese Academy of Sciences, 20A Datun Road, Chaoyang District, Beijing 10012, People's Republic of China*
[9]*Institute of Liberal Arts and Sciences, Tokushima University, Minami Jousanajima-machi 1-1, Tokushima 770-8502, Japan*
[10]*Department of Physics, Graduate School of Science, Nagoya University, Furo-cho, Chikusa-ku, Nagoya 464-8602, Japan*
[11]*University of Science and Technology, Korea, 217 Gajeong-ro, Yuseong-gu, Daejeon 34113, Republic of Korea*
[12]*Department of Physics and Astronomy, University College London, Gower Street, London WC1E 6BT, UK*
[13]*Department of Earth Science Education, Seoul National University, 1 Gwanak-ro, Gwanak-gu, Seoul 08826, Republic of Korea*
[14]*East Asian Observatory, 660 N. A'ohōkū Place, University Park, Hilo, HI 96720, USA*
[15]*Dominion Radio Astrophysical Observatory, Herzberg Astronomy and Astrophysics Research Centre, National Research Council Canada, P. O. Box 248, Penticton, BC V2A 6J9 Canada*
[16]*National Astronomical Observatory of Japan, National Institutes of Natural Sciences, Osawa, Mitaka, Tokyo 181-8588, Japan*
[17]*Department of Astronomy, Graduate School of Science, The University of Tokyo, 7-3-1 Hongo, Bunkyo-ku, Tokyo 113-0033, Japan*
[18]*Astrobiology Center, National Institutes of Natural Sciences, 2-21-1 Osawa, Mitaka, Tokyo 181-8588, Japan*
[19]*Jeremiah Horrocks Institute, University of Central Lancashire, Preston PR1 2HE, UK*

This paper has been typeset from a TEX/LATEX file prepared by the author.